Model-based Filtering of Resting-State Blood-Oxygen-Level-Dependent Signal

Ishita Rai Bansal

Master of Science Thesis

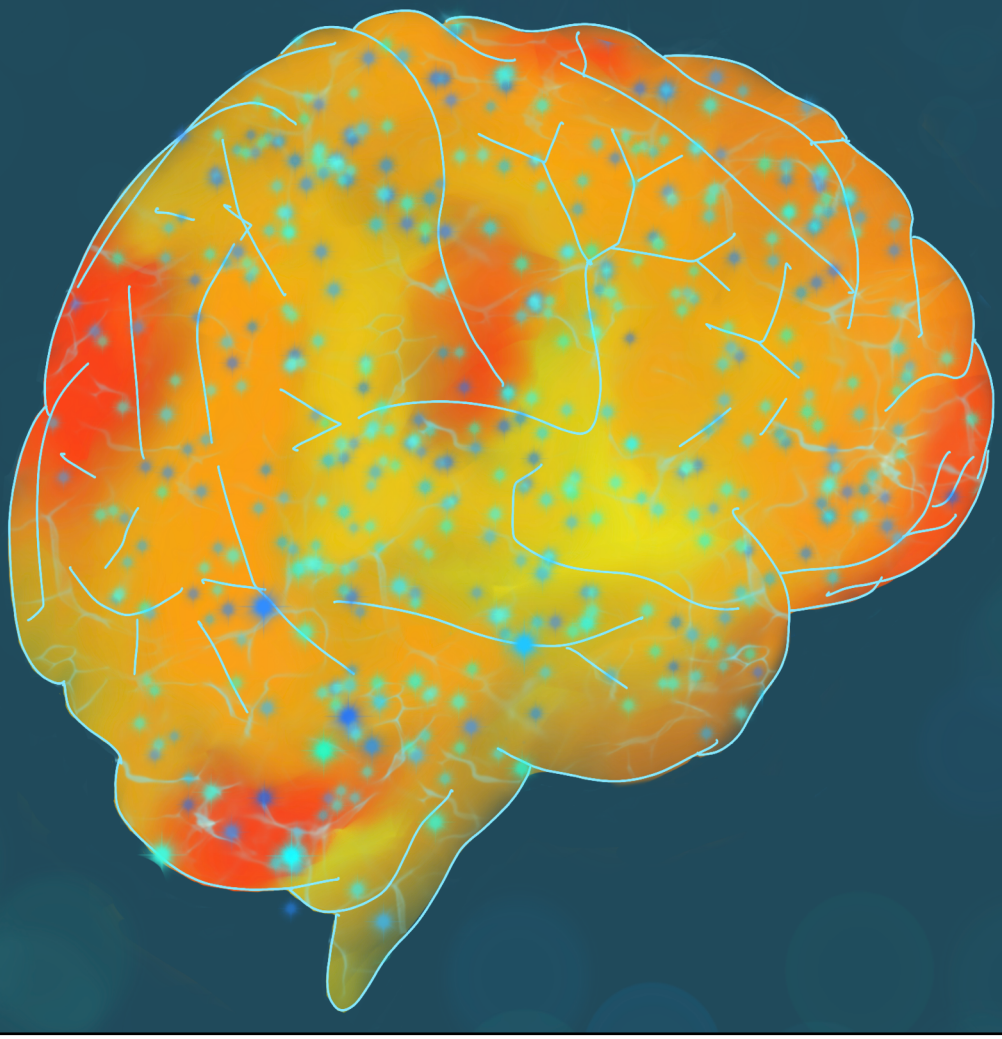

TU Delft Delft University of Technology

Delft Center for Systems and Control

Model-based Filtering of Resting-State Blood-Oxygen-Level-Dependent Signal

Master of Science Thesis

For the degree of Master of Science in Systems and Control at Delft University of Technology

Ishita Rai Bansal
(5038057)

July 6, 2021

Faculty of Mechanical, Maritime and Materials Engineering (3mE) · Delft University of Technology

Delft University of Technology
Department of
Delft Center for Systems and Control (dcsc)

The undersigned hereby certify that they have read and recommend to the Faculty of Mechanical, Maritime and Materials Engineering (3mE) for acceptance a thesis entitled

Model-based Filtering of Resting-State
Blood-Oxygen-Level-Dependent Signal

by

Ishita Rai Bansal
(5038057)

in partial fulfillment of the requirements for the degree of

Master of Science Systems and Control

Dated: _____

Supervisor(s):

_____
Dr. S. Pequito

Thesis Committee:

_____
Dr. ir. M. Mazo Espinosa

_____
Dr. S. Pequito

_____
Dr. ir. A. C. Schouten

Abstract

Resting-state functional magnetic resonance imaging (rs-fMRI) is one of the promising non-invasive technology that helps in the detection of neurodegenerative and neurological disorders, localisation of the different areas of the brain and understanding the connectivity between them. It involves the acquisition of time series of MR images while the brain is at "resting-state" and serves as a biomarker for various neurological conditions. The acquired resting-state blood-oxygen-level-dependent (BOLD) data, however, can be corrupted with various artefacts (head movements, physiological movements like breathing etc.). Several preprocessing pipelines have been developed to counter the effect of these known artefacts. However, there might be some artefacts that could not have been attenuated from the signal and might lead to incorrect assessment. Therefore, the thesis proposes model-based filtering of the minimally preprocessed (free from known artefacts) resting-state BOLD signal. It was observed that these signals have long memory dependencies. Hence, the usage of autoregressive fractional integrative process filters is proposed for this purpose.

Furthermore, the utility of the approach is demonstrated by removing the effect of white noise from a synthetic signal with statistical properties similar to the resting-state BOLD signal. Afterwards, the proposed method is implemented on the minimally preprocessed resting-state BOLD data of 98 subjects from the Human Connectome Project. The results suggest that the proposed filter, in contrast to the low-pass filter, attenuates the higher frequencies but do not eliminate them. Additionally, four different evaluation measures (power spectrum, functional connectivity using Pearson's correlation and coherence, and eigenmode analysis) were considered. The results provide evidence that the proposed method can be used as an additional step in the already existing preprocessing pipeline to mitigate some artefacts that could not have been filtered out. Besides, the results also provide evidence that the proposed scheme is suitable to capture the dynamics of resting-state BOLD signals.

Table of Contents

List of Figures

List of Tables

Acknowledgements

The two-year journey comes to an end with this last milestone. Reaching the destination topped up with some hurdles (Covid-19 being the cherry on the cake) would not have been possible without the support of many, whom I would like to express my sincere gratitude.

I wish to show my deepest gratitude to my supervisor Dr. Sérgio Pequito for providing me with an opportunity to work under his guidance. I am immensely grateful for his constant support and encouragement to push my boundaries. In addition to his broad knowledge and skill set, I really respect him for his patience and work ethics. His valuable insights at different stages of the project have always been the guiding light. I am thankful to him for all his efforts and for fulfilling my desire to do research in the field of biomedical.

I want to thank Dr. Arian Ashourvan from the University of Pennsylvania for his help, support and feedback especially in the last leg of research. I would like to pay my special regards to Dr. ir. Alfred C. Schouten and Dr. ir. M. (Manuel) Mazo Espinosa for their time and presence in my thesis committee.

The beginning and end of this journey would not have been possible without the constant love and support of my family. It was the belief and teachings of my parents that kept me motivated and provided me courage in these bizarre circumstances.

I am indebted to my friends for their presence and continuous encouragement. No amount of words are enough to thank Kriti for her support. Kriti, thank you for being the moral support system, for coping up with my emotional tantrums and for all the life lessons. The beautiful cover page of this thesis is also her masterpiece. A big thank you to you too, Mudit for always being there. He was the one who took care of my food delicacies. Both of them have been my pillar of strength all through this journey.

Last but not the least I would like to thank Tanay and Mahalakshmi, who helped me survive the Systems and Control course.

Delft, University of Technology
(5038057)
July 6, 2021

Ishita Rai Bansal

“To my mumma papa for their sacrifices and constant love”

Chapter 1

Introduction

Technological advancements have brought a revolution in the field of biomedical. Some examples include the devices that provide continuous monitoring of the biological vitals of the human body, automatic administration of the drugs to the patients and scanners to monitor the internal organs of the body. The driving force behind this development is the improvement of human health. However, there exist an unprecedented challenge for the control of chronic and neurological disease such as Alzheimer's, mental illness, stroke [3], [4].

One effective way to cure these disease is the diagnosis at an early stage [5] [6]. The neuroimaging techniques such as positron emission tomography (PET), functional magnetic resonance imaging (fMRI), electroencephalography (EEG) [7], [8], [9] provides a great potential to serve as predictive biomarkers of the neurological conditions. Due to the non-invasive nature and lack of exposure to radiations, fMRI has gained popularity for understanding the functioning of the brain [10].

At the heart of fMRI technology is the acquisition of blood-oxygen-level-dependent (BOLD) signal from the brain and its analysis. Being a data-driven approach, it is prone to contamination by artefacts. Hence, it can lead to a false-positive (indicating the presence of disease when in reality it is not present) or a false-negative (indicating the absence of disease when it is present) result. A false-positive diagnosis may result in unnecessary treatment and, a false-negative result can lead to a wrong diagnosis. Therefore, the correct analysis is highly dependent on the accuracy of the data. The thesis thus focuses on improving the preprocessing pipeline of the data.

1-1 Motivation

fMRI is a non-invasive imaging modality used for mapping the functionality of the brain. It serves as a proxy for neuronal activity by measuring the amount of blood flow. The fMRI studies assess the fluctuations in BOLD signals of the brain generated as a time series during rest or as a response to some task or externally applied stimulus. The observations by Biswal *et al.* about the temporal correlation between the BOLD fluctuations of left and right

hemispheric regions of the primary motor cortex during rest laid the foundation for a new era of research to understand the neuroanatomy by analysing the resting-state fMRI (rs-fMRI) BOLD time series data [11], which is also the area of research of this study.

As the name resting-state fMRI (rs-fMRI) suggests; it is the measurement of MR signal when the subject is in resting-state. Therefore, in these experiments, subjects are placed into the MR scanner and instructed to rest without falling asleep. rs-fMRI holds several advantages: minimal behavioural demands due to lack of explicit task, flexibility in terms of study participants and easier data acquisition, making it a good choice for its use in detecting neurological disease.

A rapid growth in rs-fMRI literature has been witnessed [12] and numerous studies illustrate its potential use in clinical applications. For instance, there have been recent studies that show the use of resting-state BOLD data to detect Autism spectrum disorders [13]. Then there are studies, which depicts that the rs-fMRI can not only help in the detection of disease but also assists in understanding the psychological behaviour of human. For example, Cao *et al.* describes how this technology can be used to study brain activity in depressed patients showing suicidal behaviour [14]. Another study illustrates its usage to detect drug abuse [15]. Barkhof *et al.* presents a review of number of clinical applications of rs-fMRI [16].

However, the resting-state BOLD data can be corrupted with confounds such as distortion due to head motion, cardiac and respiratory physiological noises, motion due to swallowing, and scanner instabilities [17]. Marcus *et al.* in [18] showed that of the total variance in resting-state BOLD data considered by them, nuisance components account for 16% of variance, motion regressors for 14%, neural components for 4% and rest is due to other artefacts.

Failure to separate these nuisance signals from the signal of interest can affect the correct analysis of resting-state BOLD data. Numerous methods have been devised to clean-up (preprocess) this data from artefacts due to head motion, slice time correction, physiological noises and hardware instabilities (Murphy *et al.*, 2013 presents a detailed review [1]). Several studies mark the importance of preprocessing of resting-state BOLD data. For instance, Grifaanti *et al.* in [19] illustrate the significance of effective cleaning of rs-fMRI data for early detection of Alzheimer's disease by comparing the generated functional connectivity alteration maps and SNR from four different cleaning methods. A non-clinical study by Craig Bennett [20] wherein a fMRI experiment was performed on a dead salmon, further demonstrated the sensitivity of the acquired data. He showed the dead salmon some photographs of humans with different emotions. Strangely, the dead salmon's brain showed evidence of activity. In other words, the fMRI scan showed that the dead salmon was thinking, thus highlighting the dangers of false positives in the data.

Even after the application of different preprocessing methods, the rs-fMRI data obtained may include signal fluctuations due to unknown sources of noise or spurious fluctuations caused by the reintroduction of some artefacts that were removed previously but got added in the later preprocessing steps [21]. To account for these limitations, the study proposes to take minimally preprocessed resting-state BOLD signals and perform time-domain filtering using a fractional parametric filter. The presence of long-term memory in these signals as captured by their autocorrelation functions led us to propose a univariate Autoregressive Fractional Integral Moving Average (ARFIMA) model [22] that is suitable to deal with (some) similar cases to capture such dependencies.

1-2 Research Questions

Fractional calculus is being widely used to model long-range dependencies of data in numerous fields, namely, signal processing, control engineering, biomedical systems and physics (Magin *et al.* in [23] provides a reference to literature in each of these domains). The long-term memory in the resting-state BOLD signals have been identified through fractal modelling (self-similarity structures) in several studies [24], [25], [26]. Herman *et al.* in [27] studied fractional properties in spontaneous BOLD fluctuations of a rat brain. Wang *et al.* used them to study the effect of different levels of isoflurane anesthesia [28].

However, this is the first time that such a fractional filter is being proposed for the filtering (modelling) of the resting-state BOLD data to the best of the authors' knowledge. To realize the objective, the study intends to find an answer to the following research questions:

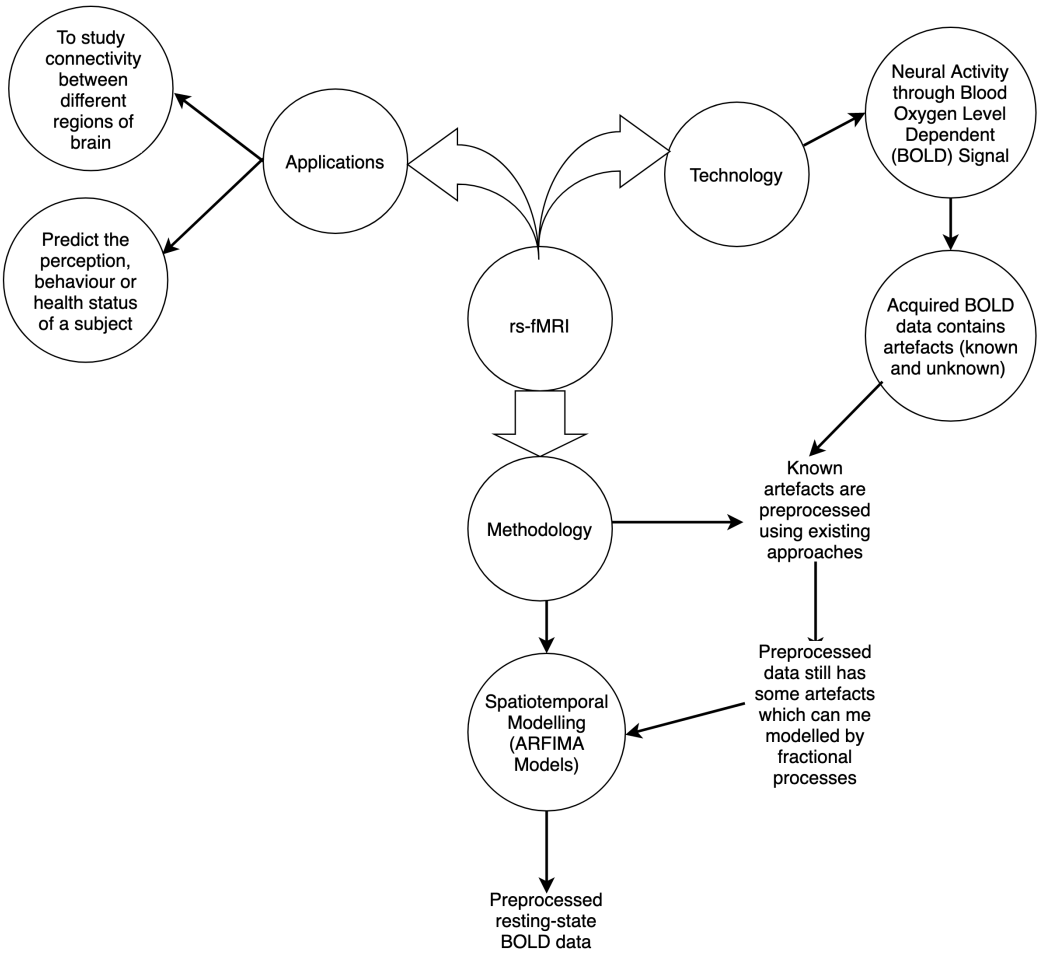

Figure 1-1: Mind map for formulating the objective of the thesis.

- Is it possible to use the concept of time series filtering to derive model-based filter to further cleanup the already preprocessed (i.e., data where identified noise sources have already been removed) resting-state BOLD signals?

- Are the properties of derived model-based filters different from the typical low pass filters?
- Is the derived filter fulfilling its objective of filtering resting-state BOLD data, not at the expense of introducing spurious functional connectivity between different brain regions?

The entire process of reaching to the formulation of defined objective and research questions is structured in Figure 1-1.

1-3 Research Contributions

Technological innovations have made available numerous sensors that can provide finer details on the inner body parts and organs. The analysis of the data from sensors can help and improve the diagnosis. However, the acquired biomedical signals contain different types of noise. A major part of the research nowadays looks into methods to extract clinically viable information. On the similar grounds, this study provides a method to mitigate the effect of the leftover noise from the resting-state fMRI data.

The proposed filter is limited to the field of resting-state BOLD signals for this research. Nonetheless, its scope can be extended to other biomedical signals or even signals in other domains that have the long-term memory structure such as financial time series, electroencephalography signal and underwater signal [29]. As noticed in this study, the proposed filters are suitable for modelling the low-frequencies, therefore, their usage can be advantageous where a low-frequency signal is of paramount interest.

This study as part of Master's thesis is not limited to the degree, rather we have also submitted a paper based on the conducted research in the PLoS One journal. The implementation of the proposed method (i.e., the MATLAB code) can be accessed here: link to git repository.

1-4 Thesis Outline

The report is organised as follows: Chapter 2 provides a brief introduction on the principle of rs-fMRI, its interpretation as time series, the outline of the conducted literature survey on the presence of artefacts in the resting-state BOLD data and the concepts of time series filtering. Chapter 3 introduces the dataset used in the study and discusses the proposed methodology to fulfil the objective of the thesis. Chapter 4 analyses the results obtained after implementation of the proposed method, and finally, the report concludes with a discussion on limitations and future work of the study in Chapter 5.

Chapter 2

Background Information

This chapter begins with a brief introduction on the principle of MRI followed by a discussion on the principle and data acquisition of rs-fMRI. Further, it presents an overview of the previously proposed methods to mitigate the effect of artefacts in the rs-fMRI data. The chapter also discusses the concepts of modelling of time series. The concepts discussed here are used in the latter part of the research to formulate the proposed method.

2-1 Functional Magnetic Resonance Imaging

Functional magnetic resonance imaging (fMRI) is a non-invasive imaging technique used to examine the functional connectivity of the brain and to study its neuronal activity. It consists of acquiring a sequence of magnetic resonance (MR) images over a course of time (Figure 2-1). Therefore, the primary building step towards understanding the acquisition of fMRI data is studying the principle and acquisition of MR images.

2-1-1 Magnetic Resonance Imaging

Magnetic resonance is the effect that is observed when radiofrequency electromagnetic waves perturb a magnetic dipole placed in a stronger magnetic field. This phenomenon occurs in nuclei possessing non zero spins (i.e., the number of protons in a nucleus is not equal to the number of neutrons). One such nucleus available in abundance in the human body is the hydrogen atom (^{1}H). Therefore, in magnetic resonance imaging (MRI) of the human body, the MR signal arising from dipoles of the hydrogen atom is looked upon.

The MR imaging process begins with placing the subject in an electromagnet having a strong magnetic field, B_0 of the order of 1.5 to 7T. The presence of this strong magnetic field exerts a force on the hydrogen atoms aligning them in parallel or anti parallel direction to the main magnetic field. As a result, a net magnetic moment, M is created parallel to B_0 as shown in Figure 2-2. This process is similar to how a small bar magnet aligns itself to the local

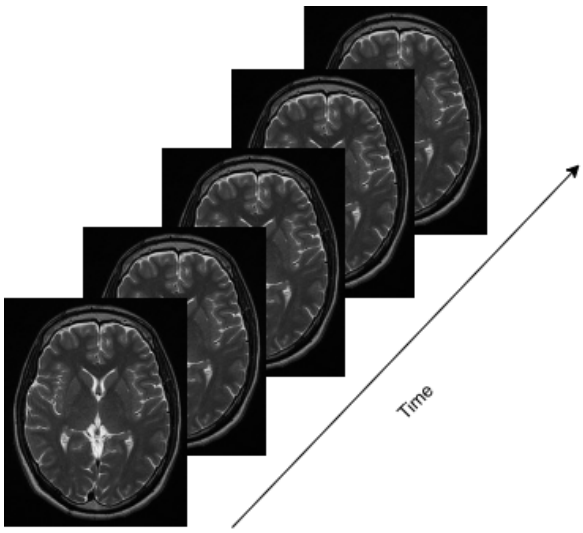

Figure 2-1: fMRI technology: Acquistion of MR images over a period of time.

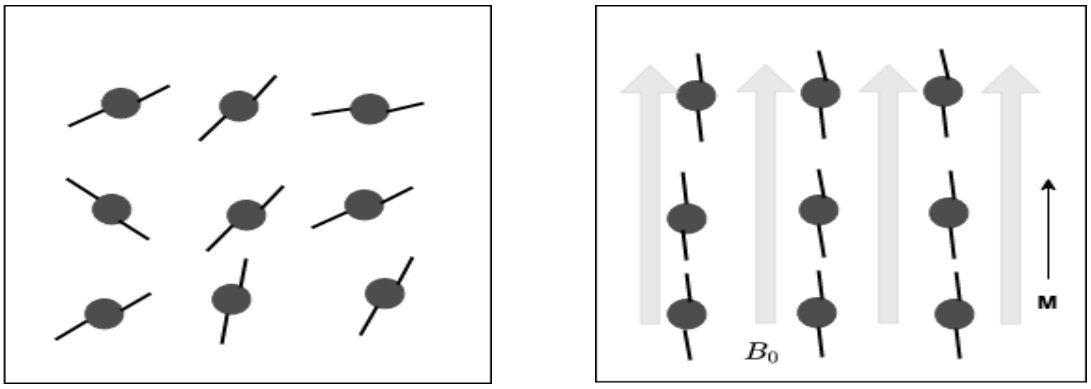

(a) **(b)**

Figure 2-2: Alignment of nuclear spins in presence of strong magnetic field. (a) In absence of strong magnetic field, hydrogen nuclei are randomly aligned. (b) After application of magnetic field B_0, net magnetic moment M is developed in the direction of applied magnetic field.

magnetic field. In this state, the system is said to be in the state of equilibrium. Now, a radio frequency (RF) pulse is applied to the system leading to the excitation of the nuclei and they start precessing in phase. This excitation is only possible at a resonance frequency termed as Larmor frequency given by

$$\omega = \gamma B_0, \tag{2-1}$$

where ω is the Larmor frequency, γ is the gyromagnetic ratio, and B_0 is the external applied magnetic field. At this frequency, the RF pulse, B_{rf} tilts the net magnetic moment M away from B_0. This effect on magnetic moment due to RF pulse can be seen in Figure 2-3. In this scenario, the system is said to be in a non-equilibrium state. Once the RF pulse is removed, the hydrogen nuclei tend to return to their equilibrium state by emitting radio waves, which induce a current in the receiver coil. The emitted RF signal is referred to as free-induction decay (FID) response signal, and the induced current provides the MR signal.

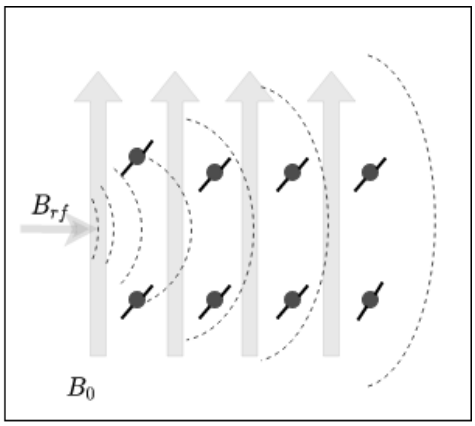

Figure 2-3: RF pulse B_{rf} tilts the net magnetic moment M away from B_0.

The relaxation of hydrogen nuclei back to their original state can be described by two exponential processes with time constants T1 and T2. The exponential process with time constant T1, also known as *longitudinal relaxation*, measures the time required for the relaxation of nuclei back to their equilibrium state (i.e., realign itself in the direction of the applied magnetic field). The *transverse relaxation* defined by the time constant, T2 measures the time required for the FID response signal to decay i.e., time taken by nuclei to dephase in the transverse direction (which were earlier precessing in phase). Ideally, the transverse relaxation follows an exponential decay; however, the presence of inhomogeneities (tissue-related or magnet-related) in the applied magnetic field aids in speeding up the process of transverse relaxation. The time constant in this case is termed as $T2^*$. The size of these tissue-related inhomogeneities in the brain is dependent on its physiological state (i.e., the composition of blood supply to the brain), which in turn is dependent on the neural activity and is measured by the $T2^*$ parameter. $T2^*$ thus, is an indirect measure of neural activity.

This section is a basic description of the process of MRI. The detailed description of the same and the mathematics behind the MR image formation can be found in textbooks [30], [31]).

2-1-2 Blood-Oxygen-Level-Dependent (BOLD) fMRI

The technique which forms a link between the neural activity of the brain and measured $T2^*$ is the mechanism called *blood-oxygen-level-dependent* (BOLD) contrast. In fMRI, these BOLD signals are the signal of interest.

fMRI study is based on the fact that the oxygenated and deoxygenated haemoglobin have different magnetic susceptibilities. Deoxyhemoglobin (dHb) being paramagnetic introduces inhomogeneities in the local field leading to faster dephasing of hydrogen nuclei spins which in turn shortens $T2^*$ and thus suppresses the intensity of the received MR signal. This effect of dHb on $T2^*$ was first observed by Ogawa *et al.* in their study on the rodent brain [32]. They concluded that the BOLD contrast varies with change in blood oxygen and, thus, provides an additional feature to study brain neural activity using MRI [33]. This formed the basis for the analysis of BOLD signals in fMRI.

Attwell and Laughlin in 2001 [34] noticed that cerebral metabolic rate of oxygen consumption ($CMRO_2$) increases with an increase in neural activity. This implies that when the blood reaches the area with increased neural activity, more oxygen is loaded from the passing haemoglobin in the local venous blood vessel leading to increased dHb in the local blood vessel, hence, shortening $T2^*$ and thus, reducing the BOLD signal.

However, earlier studies [33] and [35] show that the BOLD signal increases in response to neural activity (i.e., decrease in dHb concentration should be observed). The observed decrease in dHb concentration is due to an increase in cerebral blood flow (CBF) and cerebral blood volume (CBV) in response to increased neural activity. Increased neural activity leads to increased demand for oxygen and, hence, oxyhaemoglobin is oversupplied to the activated area, thus, resulting in the decrease of dHb concentration (i.e., increase in the magnitude of BOLD signal).

The explanation of these two contradicting scenarios is based on the fact proven by Hoge *et al.* that the resulting increase in CBF in response to neural activity is two times the increase in $CMRO_2$ [36]. Hence, an overall increase in BOLD signal is observed with increased brain activity. Therefore, in a simplified manner, the activation of neurons leads to an increase in local blood oxygen and hence, the amplitude of BOLD signal increases [37], [38]. Figure 2-4 shows a schematic representation between increase in neural activity and BOLD signal. Hence, the change in metabolic demand of neurons leads to the observed fluctuations in the acquired BOLD signal, as can be seen in Figure 2-5.

2-1-3 Fluctuations in resting-state BOLD fMRI

The fluctuations in resting-state BOLD signal consists of contribution not only due to true neural activity of the brain but also from several physiological and non-physiological sources. Physiological sources of noise include artefacts arising from both neuronal and non-neuronal components such as due to cardiac and respiratory cycles as well as blood pressure oscillations [1], [39]. Non physiological noises include drift, slice time correction, head motion and scanner instabilities [1], [40], [41].

Inability to properly account for these confounds or noises present in the resting-state BOLD signal can have a considerable effect their analysis. For instance, Van Dijk *et al.* in [42] shows

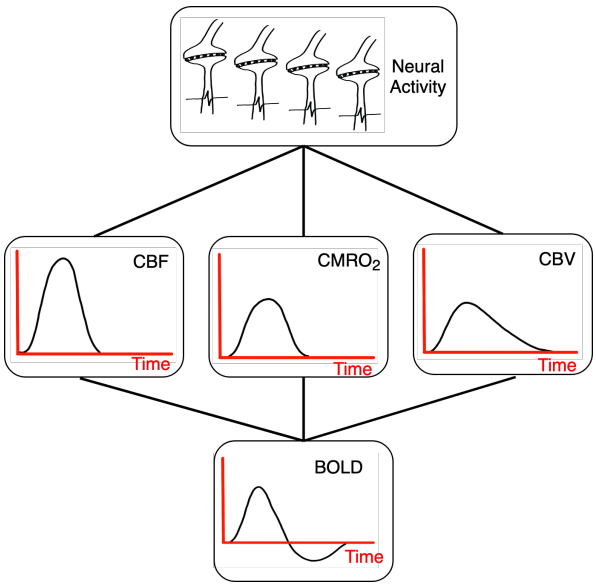

Figure 2-4: Representation of relationship between increase in neural activity and magnitude of BOLD signal (Modified from [1]).

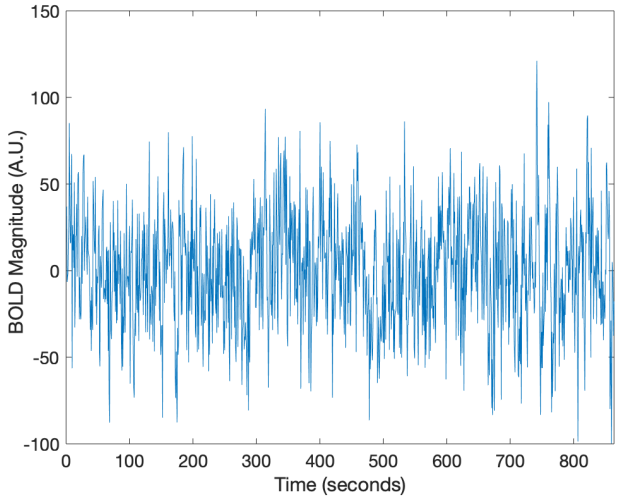

Figure 2-5: Time series of resting-state BOLD signal from one of the regions of brain.

the effect of head motion on the functional connectivity measures of rs-fMRI. These nuisance components pose a risk of artificially influencing functional connectivity between different brain regions and thus yielding spurious results [39]. The influence of nuisance components may vary and depend on the number of factors [40]. Therefore, an effective preprocessing pipeline is needed for the separation of true neural data from the acquired noisy resting-state BOLD signal.

Existing Denoising Methods in resting-state BOLD fMRI

Many denoising approaches have been developed for isolating true neural activity from acquired rs-fMRI data. These include the following: (i) model-based approaches which estimate contributions to BOLD signal from physiological sources [43] or due to head motion [44]; (ii) data-driven approaches which estimate noise from data using independent component analysis [40]; (iii) scrubbing (removing) time points acquired during the period of high motion [45]; (iv) combining data-driven methods with multiecho data acquisitions, which were observed to perform better in terms of removing noise from resting-state BOLD signal fluctuations [46].

In resting-state fMRI, the change in amplitude of BOLD signal is observed over time (Figure 2-5 shows an example of resting-state BOLD time series). Therefore, it presents a great potential to interpret this data as time series and perform filtering. The research thus, is aimed at exploring methods to achieve its objective of removing confounds from resting-state BOLD data by interpreting it as time series. The following section highlights some of the basic concepts of time series modelling.

2-2 Time Series Modelling

Informally, a *time series* can be described as a set of observations taken sequentially in time [47]. If this set is discrete, the time series is said to be *discrete time series*.

Definition 2-2.1 (Time Series [47])**.** A *time series* z_t of N successive observations $z_{t_1}, z_{t_2}, \ldots, z_{t_N}$, where, $z_{t_n} \in \mathbb{C}$, is a realization from a set of infinite time series that could have been generated by the stochastic process Z_t .

As the time series is a realization of a stochastic process and it will be clear from the context of discussion what is being referred to, therefore for ease, no notational distinction is made between both of these concepts. The modelling of time series is generally done with the assumption of time-invariant statistical properties widely known as stationarity. Another important property of the time series is based on the measure of dependency or correlation and is known as long-memory and short-memory processes. The following sections provide a brief description of these properties of time series.

2-2-1 Stationary time series

Stationarity can be defined as a sort of regularity that may exist over time in the behaviour of a time series [48]. Mathematically, it can be defined as follows.

Definition 2-2.2 (Strictly Stationarity [48])**.** Stationarity is defined as a series having statistical properties (i.e. mean, variance and covariance) that do not change over time. Thus, a time series Z_t is strictly stationary if, for $t = \{1, \ldots, n\} \subseteq \mathbb{N}$ and $\tau \subseteq \mathbb{Z}$, its joint distribution function is invariant under a shift in time:

$$P\left[Z_1 \leq \alpha_1, \ldots, Z_n \leq \alpha_n\right] = P\left[Z_{1+\tau} \leq \alpha_1, \ldots, Z_{n+\tau} \leq \alpha_n\right] \quad \forall n \in \mathbb{N} \ . \tag{2-2}$$

A slightly weaker version of stationarity known as *Wide Sense Stationarity.*

Definition 2-2.3 (Wide Sense Stationary (WSS) [49])**.** WSS is a weaker notion of stationarity. A time series $\{Z_t : t \in \mathbb{N}\}$ is termed as WSS if its mean and covariance are time invariant i.e., they do not change over time and the variance is finite for all time instants, i.e., $\forall t, \tau \in \mathbb{N}$:

$$\text{Mean: } \mathbb{E}[Z_t] = \mu < \infty, \tag{2-3}$$

$$\text{Covariance: } \mathbb{E}[(Z_t - \mu)(X_{t+\tau} - \mu)] = \gamma_0 \quad \textit{and} \tag{2-4}$$

$$\text{Variance: } \mathbb{E}\left[(Z_t - \mu)^2\right] = \gamma_\tau. \tag{2-5}$$

2-2-2 Long memory and short memory time series

One of the measures of the dependency of time series is correlation between values of time series at different time instants. This correlation of the time series with itself can be measured by sample autocorrelation function.

Definition 2-2.4 (Autocorrelation Function (ACF) [47])**.** ACF defines the correlation of a signal with its delayed copy and is given by

$$\rho_k = \frac{\sum_{t=1}^{n-k}\left(Z_t - \bar{Z}\right)\left(Z_{t+k} - \bar{Z}\right)}{\sum_{t=1}^{n}\left(Z_t - \bar{Z}\right)^2}, \tag{2-6}$$

where ρ_k is the sample autocorrelation function at lag k, Z_t is the observed time series, and $\bar{Z}$ is the mean of the time series [47].

The processes which exhibit *short-memory* property have an autocorrelation function that declines exponentially as the distance between time increases [29]. However, there exists time series which possess the *long-range dependence (LRD)* structure or *long-memory* property, i.e., there is strong coupling (correlation) between signal and its delayed copy. Hence, its sampled autocorrelation function has an inverse power law behaviour (i.e., slowly declining autocorrelation function) which is the case in the sample autocorrelation plot of the resting-state BOLD time series from one of the regions of the brain, illustrated in Figure 2-6. The blue lines in the figure indicate the default 95% confidence interval calculated based on the assumption that the process is white noise [47]. If the autocorrelation value is within this region, it means the coefficient is statistically insignificant and can be ignored.

One of the common approaches to model this LRD structure is differencing the time series. A set of model that uses the concept of fractional differencing for modelling of long memory time series is Autoregressive Fractional Integral Moving Average (ARFIMA) model.

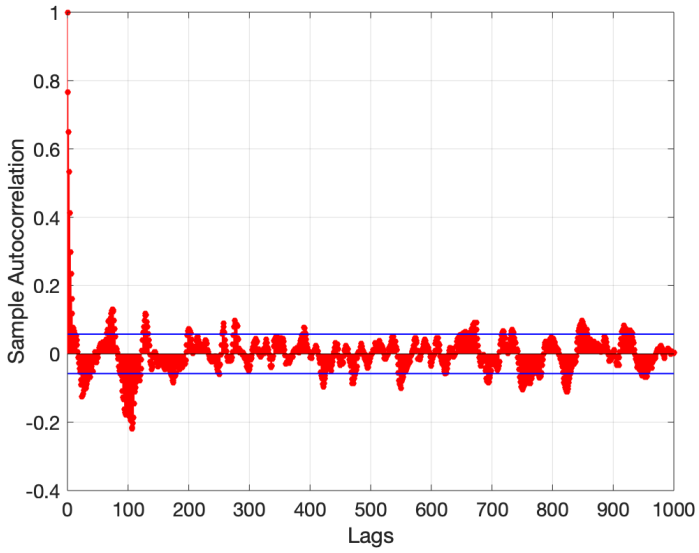

Figure 2-6: Sample Autocorrelation plot of the resting-state BOLD signal from one of the regions of brain. The inverse power law behavior of the plot depicts the presence of long-memory in the signal.

2-2-3 ARFIMA modelling

ARFIMA (p, d, q) modelling is an extension to conventional Autoregressive Moving Average (ARMA) (p, q) by incorporating a fractional differencing term in them. The primitive knowledge of the ARFIMA processes was given by Granger *et al.* [22]. Some of the known processes that exhibit LRD property are: financial time series, electroencephalography signal, and underwater signal [29]. Although integral differencing can also model the LRD property in the data, however, economists believe that this may lead to losing some important information from the data [22]. Xiu *et al.* in [50] gives mathematical proof of how integer order differencing might lead to over differencing and hence, highlights the importance of fractional differencing. Henceforth, the existing ARMA models, which are capable of modelling the short-memory time series are extended to ARFIMA models thus, capturing the long run dependencies and non-stationarity among the data.

A complete mathematical theory about fractional calculus, fractional differential equations and fractional integrals can be found in literature [51], and [52]. This section highlights some basic concepts of the ARFIMA (p, d, q) modelling.

ARMA (p, q) model

Consider a stationary stochastic process Z_t consisting of $z_{t_1}, z_{t_2}, \ldots, z_{t_m}$, M, successive observations made at equidistant time intervals. Using ARMA (p, q) modelling, the process Z_t can be modelled as

$$\phi(B)\left(Z_t - \mu\right) = \psi(B)\varepsilon_t, \tag{2-7}$$

where μ is the mean of the process Z_t, ε_t is the independent and identically distributed (i.i.d.) noise with mean zero and bounded variance. In particular, the noise can be assumed

to be white gaussian noise, which is described by a normal distribution with zero mean and variance σ_ε^2, denoted by $\varepsilon_t \sim WN\left(0, \sigma_\varepsilon^2\right)$. Additionally, $\phi(B)$ and $\psi(B)$ are the autoregressive and moving average operators respectively, and B is the backward shift operator defined as $BZ_t = Z_{t-1}$, i.e., $B^i Z_t = Z_{t-i}$.

The autoregressive and moving average operators represented in terms of backshift operator are defined as

$$\phi(B) = 1 - B\phi_1 - B^2\phi_2 - \cdots - B^p\phi_p \tag{2-8}$$

and

$$\psi(B) = 1 + B\psi_1 + B^2\psi_2 + \cdots + B^q\psi_q, \tag{2-9}$$

where $\phi_1, \phi_2, \ldots, \phi_p \in \mathbb{R}$ are the autoregressive parameters, $p \in \mathbb{N}$ is the order of the autoregressive component, $\psi_1, \psi_2, \ldots, \psi_q \in \mathbb{R}$ are the moving average parameters, and $q \in \mathbb{N}$ is the order of the moving average component.

The ARMA (p, q) model in Equation 2-7 can be termed as purely *autoregressive* or AR (p) model if $q = 0$. An autoregressive process is defined as a process in which the current value of a process is a linear combination of its past values and a white noise sequence and its order p highlights the number of the past steps needed to forecast the current value [48]. Mathematically, the AR (p) process can be defined as

$$\left(1 - \phi_1 B - \phi_2 B^2 - \ldots - \phi_p B^p\right)(Z_t - \mu) = \varepsilon_t \tag{2-10}$$

$$\implies Z_t = \mu + \phi_1 (Z_{t-1} - \mu) + \phi_2 (Z_{t-2} - \mu) + \ldots + \phi_p (Z_{t-p} - \mu) + \varepsilon_t, \tag{2-11}$$

with $\phi_1, \phi_2, \ldots, \phi_p \in \mathbb{R}$, $p \in \mathbb{N}$ is the order of the AR process, μ is the mean of the process Z_t, and $\varepsilon_t \sim WN\left(0, \sigma_\varepsilon^2\right)$.

Similarly, the ARMA (p, q) model in Equation 2-7 can be termed as purely *moving average* or MA (q) model if $p = 0$. A moving average process is defined as a process which is formed by a linear combination of white noise sequence [48]. Mathematically, the MA (q) process can be defined as

$$Z_t = \left(1 + \psi_1 B + \psi_2 B^2 + \ldots + \psi_q B^q\right)\varepsilon_t \tag{2-12}$$

$$\implies Z_t = \varepsilon_t + \psi_1\varepsilon_{t-1} + \psi_2\varepsilon_{t-2} + \ldots + \psi_q\varepsilon_{t-q}, \tag{2-13}$$

where $\psi_1, \psi_2, \ldots, \psi_q \in \mathbb{R}$, $q \in \mathbb{N}$ is the order of the MA process, and $\varepsilon_t \sim WN\left(0, \sigma_\varepsilon^2\right)$.

However, the ARMA (p, q) processes are known as short-memory processes (i.e., ACF ρ_k of such processes decays exponentially fast as $h \to \infty$). In order to model the long-memory processes with these general models, fractional differencing is employed.

Autoregressive Fractional Integral Moving Average (ARFIMA) (p, d, q) model

Using ARFIMA (p, d, q) modelling the stochastic process, Z_t, can be modelled as [47], [29], [53]:

$$\phi(B)(1 - B)^d (Z_t - \mu) = \psi(B)\varepsilon_t, \tag{2-14}$$

where μ is the mean of process Z_t, ε_t is the white noise process with mean zero and variance σ_ε^2 defined as $\varepsilon_t \sim WN\left(0, \sigma_\varepsilon^2\right)$, $(1 - B)^d$ is called the difference operator, $d \in \mathbb{R}_+$ is the *fractional-order* difference parameter, and $\phi(B)$ and $\psi(B)$ are the autoregressive and moving

average operators respectively as defined in Equation 2-8 and 2-9. The difference operator can be represented in terms of gamma function by solving its binomial expansion [50], i.e.,

$$(1-B)^d = \sum_{k=0}^{\infty} \frac{\Gamma(k-d)}{\Gamma(k+1)\Gamma(-d)} B^k, \tag{2-15}$$

where $\Gamma(\cdot)$ is the gamma function defined as follows.

Definition 2-2.5 (Gamma Function, represented by Γ [54])**.** It is a generalisation of a factorial function for real number and complex number with real part greater than 1. The mathematical definition of gamma function is

$$\Gamma(z) = \int_0^{\infty} x^{z-1} e^{-x} dx, \quad \mathfrak{Re}(z) > 0. \tag{2-16}$$

For a positive integer n, it is given as: $\Gamma(n) = (n-1)!$.

Properties of Gamma Function: Following are some of the important properties of gamma function, proof of which can be found in [54].

- $\Gamma(z+1) = z\Gamma(z)$.
- $\Gamma(1) = 1$, $\Gamma(1/2) = \sqrt{\pi}$ and $\Gamma(-1/2) = 2\sqrt{\pi}$.
- Gamma function is undefined for negative integers.

Procedure for modelling of ARFIMA (p, d, q) processes

The modelling of ARFIMA (p, d, q) process where p denotes the number of autoregressive parameters, d represents the order of fractional differencing and q denotes the number of moving average parameters, is a three-step procedure as illustrated by the block diagram in Figure 2-7. First, fractional differencing parameter d is determined from the long-term memory present in the process. There are number of methods for estimation of d such as Hurst parameter, ordinary least square, maximum likelihood, Robinson estimator, methods based on log-periodogram [55], [56]. Second, fractional differencing procedure on the time series Z_t is employed to obtain a stationary and short-memory process, W_t, which can be modelled by general ARMA process. Finally, the parameters p, q and the coefficients ϕ, ψ of the ARMA (p, q) process are estimated from W_t to obtain an ARFIMA modelled process X_t.

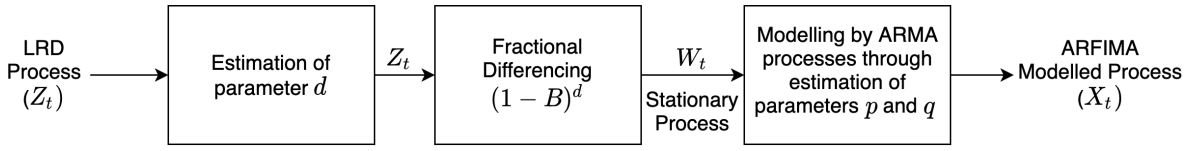

Figure 2-7: Block diagram depicting three step procedure for modelling of ARFIMA (p, d, q) process.

Fractional differencing procedure

For time series Z_t, fractional differencing of order d can be given by the formula

$$W_t = (1-B)^d Z_t, \tag{2-17}$$

where Z_t is called an integrated series with parameter d and is denoted as $Z_t \sim I(d)$. The binomial expansion of $(1-B)^d$ is given as:

$$\begin{aligned}(1-B)^d &= \sum_{k=0}^{\infty}(-1)^k \begin{pmatrix} d \\ k \end{pmatrix} B^k \\ &= \sum_{k=0}^{\infty} \frac{\Gamma(k-d)}{\Gamma(k+1)\Gamma(-d)} B^k \\ &= 1 - \mathrm{d}B + \mathrm{d}(d-1)B^2/2! - \cdots .\end{aligned} \tag{2-18}$$

After determining the value of d, the only independent parameter in Equation 2-18 is k, and let it be represented as $f(k)$. Therefore, Equation 2-17 becomes

$$W_t = \left(\sum_{k=0}^{\infty} f(k)B^k\right) Z_t. \tag{2-19}$$

Hence,

$$\begin{aligned} W_t &= \left(f(0)B^0 + f(1)B^1 + f(2)B^2 + \cdots + f(i)B^i + \cdots\right) Z_t \\ \implies W_t &= f(0)Z_t + f(1)Z_{t-1} + f(2)Z_{t-2} + \cdots + f(i)Z_{t-i} + \cdots , \end{aligned} \tag{2-20}$$

where,

$$\begin{aligned} t = 0: &\quad W_0 = f(0)Z_0 \\ t = 1: &\quad W_1 = f(0)Z_1 + f(1)Z_0 \\ \vdots &\quad \vdots \\ t = N: &\quad W_N = f(0)Z_N + f(1)Z_{N-1} + f(2)Z_{N-2} + \cdots + f(N-1)Z_1 + f(N)Z_0. \end{aligned}$$

The above procedure can be expressed using matrix and thus fractional differencing can be achieved using matrix multiplication, i.e., by computing $W = Z \times F$, where $W = \begin{bmatrix} W_0 & W_1 & \dots & W_N \end{bmatrix}_{1\times N+1}$, $Z = \begin{bmatrix} Z_0 & Z_1 & \dots & Z_N \end{bmatrix}_{1\times N+1}$ and

$$F = \begin{bmatrix} f(0) & f(1) & f(2) & f(3) & \dots & f(N-1) & f(N) \\ 0 & f(0) & f(1) & f(2) & \dots & \dots & \dots \\ 0 & 0 & f(0) & f(1) & \dots & f(2) & f(3) \\ 0 & 0 & 0 & f(0) & \dots & f(1) & f(2) \\ 0 & 0 & 0 & 0 & \dots & f(0) & f(1) \\ 0 & 0 & 0 & 0 & 0 & \dots & f(0) \end{bmatrix}_{N+1\times N+1} .$$

The fractional differencing of the time series in this study is implemented using the procedure described above. Further, Figure 2-8 shows the effect of fractional differencing for $d = 0.4$ on the ACF of a randomly simulated time series having long-memory property. Exponentially declining ACF in Figure 2-8b depicts that the fractional differencing is able to capture

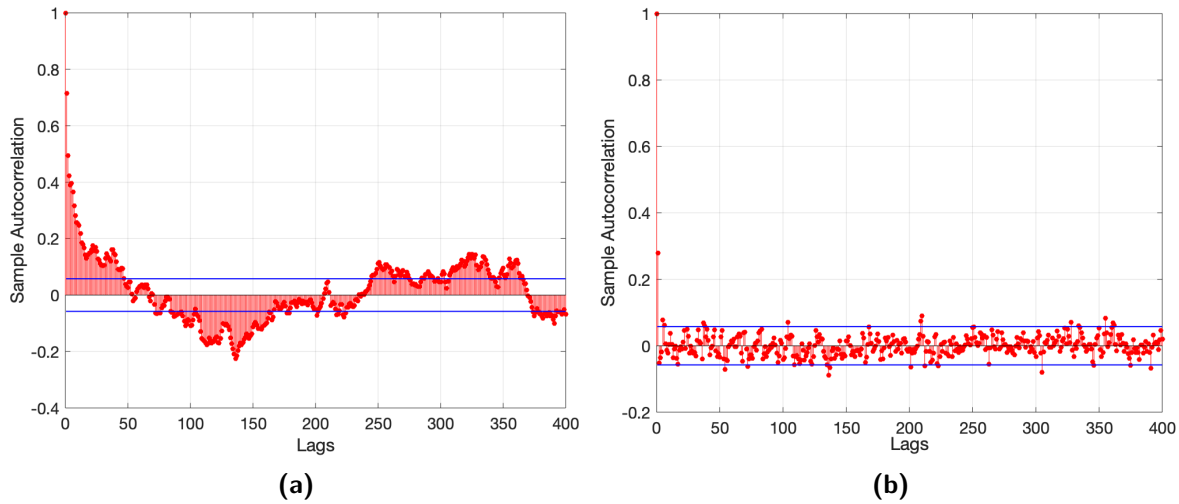

Figure 2-8: ACF of simulated ARFIMA $(1, d, 1)$ process with $\phi = 0.5$ and $\psi = 0.2$. (a) Slowly declining ACF of ARFIMA $(1, 0, 1)$ time series. (b) Exponentially declining ACF of fractionally differenced time series modelled by ARFIMA $(1, 0.4, 1)$.

the long-term dependency which was present in the series earlier (as can be observed from Figure 2-8a).

Drawing motivation from the observation that the resting-state BOLD signal has properties of long memory processes and using the theory of ARFIMA models to model such processes (discussed in this chapter), Chapter 3 aims to provide a methodology for using these parametric models to mathematically model the minimally preprocessed resting-state BOLD data.

Chapter 3

Proposed Methodology

This chapter introduces the dataset used for the study. Further, it presents the method proposed to perform ARFIMA $(1, d, 0)$ (model-based) filtering on the resting-state BOLD signals. Additionally, this chapter also discusses the metrics which will later be used in Chapter 4 to evaluate and analyse the performance of the proposed methodology.

3-1 Dataset

The research utilises resting-state fMRI (rs-fMRI) dataset from the Human Connectome Project (HCP), which was minimally preprocessed by a team at the University of Pennsylvania. Both [57] and [58] provide a detailed description of the acquisition protocol. Briefly, the data was acquired in four runs, each of approximately 15 minutes. There were two sessions, each consisting of two runs. Within each session, in one run, phase encoding was done in the right-to-left (RL) direction and left-to-right (LR) in another run. Participants were instructed to relax with their eyes open and visual fixation on a projected bright cross-hair on a dark background (and in a darkened room). The data was acquired on HCP 3T Siemens "Connectome Skyra" scanner and was part of the HCP S1200 release. rs-fMRI data was obtained using blood-oxygen-level-dependent (BOLD) contrast sensitive gradient-echo echo-planar imaging having a multiband factor of 8, TE of 33.1 ms, TR of 720 ms, spatial resolution of 2 mm isotropic voxels and a flip angle of 52 deg.

The acquisition of fMRI data requires the division of a brain into voxels. Voxels are cubic volumes that span the 3D volume of the brain. Each voxel has a spatial location (pertaining to the area of the brain it lies in) and a number (intensity of the measured MR signal) associated with it. The brain is said to be composed of these $100,000$ equally spaced small cubes known as voxels as shown in Figure 3-1 wherein the cyan-coloured cube is one of the voxels. In BOLD fMRI, the time series of BOLD signal is the intensity of measured MR signal from each of these voxels over a period of time as shown in Figure 3-2.

Therefore, fMRI involves interpretation of the time series of each of the $100,000$ different voxels which is a computationally expensive process. Hence, in order to simplify the process,

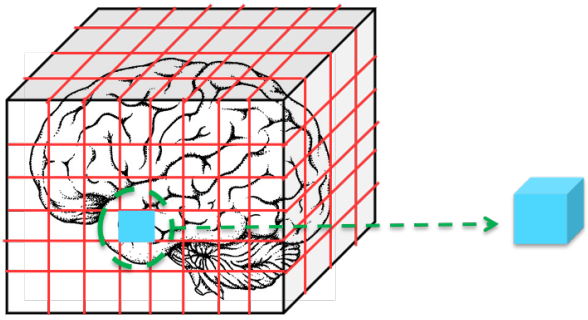

Figure 3-1: Parcellation of brain into equally spaced voxels. Cyan colored cube shows one of the voxel of a brain.

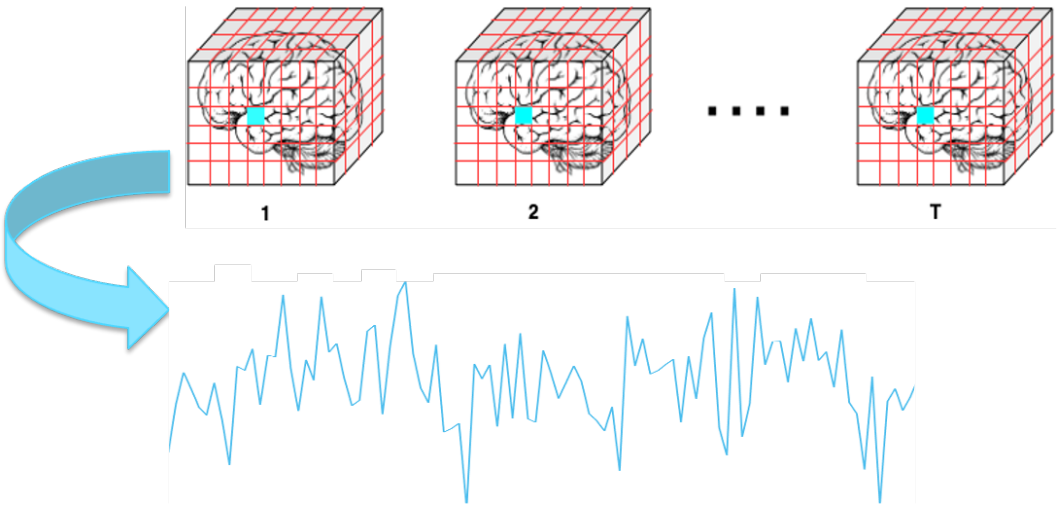

Figure 3-2: Prinicple of fMRI: tracking the measured intensity of a voxel (cyan colored time series is the timeseries of intensity of a voxel) over a period of time, $k = 1, \ldots, T$.

some voxels are grouped together to form *Regions of Interest (ROIs)*. The voxels can be grouped by creating a small search space (for instance, a sphere with radius of N voxels or a $N \times N$ square matrix of voxels) or based on anatomical atlases (AAL atlas [59], Talairach Atlas [60], to name a few). Combining voxels to form ROIs helps in decreasing the number of $100,000$ time series to a lesser number thus reducing multiple analysis [61]. Therefore, n resting-state BOLD time series corresponding to n ROIs are obtained.

The HCP dataset (used for the study) consists of data from 98 subjects with least head movement artefacts, and the brain of each subject is cortically parcellated [62] into $n(= 100)$ brain regions. Therefore, a total of $n(= 100)$ resting-state BOLD time series with 1200 data points for each of the four runs of each subject are considered in this research.

3-1-1 Preprocessing

The HCP resting-state BOLD underwent two-step preprocessing at the University of Pennsylvania to remove the effect of known sources of noise which is summarised in Figure 3-3. The first step utilises FMRIB's ICA-based Xnoiseifier (ICA-FIX) methodology [63], [64] to remove artefacts related to motion and nuisance signals. This methodology consists of first decomposing the resting-state BOLD signal into various independent components using MELODIC (Multivariate Exploratory Linear Optimised Decomposition into Independent Components) [65]. Afterwards, the method of FIX is employed for the identification of ICA components corresponding to artefacts. Finally, the identified artefactual components are subtracted from the BOLD data for denoising. This is followed by global signal normalisation, in which the mean global signal is removed from the data to cancel the artefacts due to global effects on local resting-state BOLD signals. These global effects may originate from physiological processes (pulsation, swallowing) or variations in scanner sensitivity [66].

The minimally preprocessesd data thus obtained is further used to fulfil the objective of the thesis i.e., to remove fluctuations due to leftover confounds such as unstructured noise from the resting-state BOLD signals. In the context of this study, whenever we refer to the resting-state BOLD dataset, we mean the minimally preprocessed signals, and filtered BOLD signals imply the signals obtained after ARFIMA filtering.

3-2 Proposed ARFIMA (model-based) filtering

Each resting-state BOLD time series undergoes the Autoregressive Fractional Integral Moving Average (ARFIMA) (model-based) filtering separately. Let Z_t^i be a minimally preprocessed time series from the ith ROI of the brain. The objective is to model this time series using autoregressive fractional integral moving average (ARFIMA) model[29], [53], [47] and remove any unwanted fluctuations due to artefacts that could not be removed earlier or that could have been added in the preprocessing steps. Therefore, an ARFIMA (p, d, q) model is obtained, where the parameters p, d and q describe the order of the autoregressive, fractional integrative, and moving average component respectively. Specifically, an ARFIMA (p, d, q) is described by

$$\phi(B)(1 - B)^d (Z_t - \mu) = \psi(B)\varepsilon_t, \tag{3-1}$$

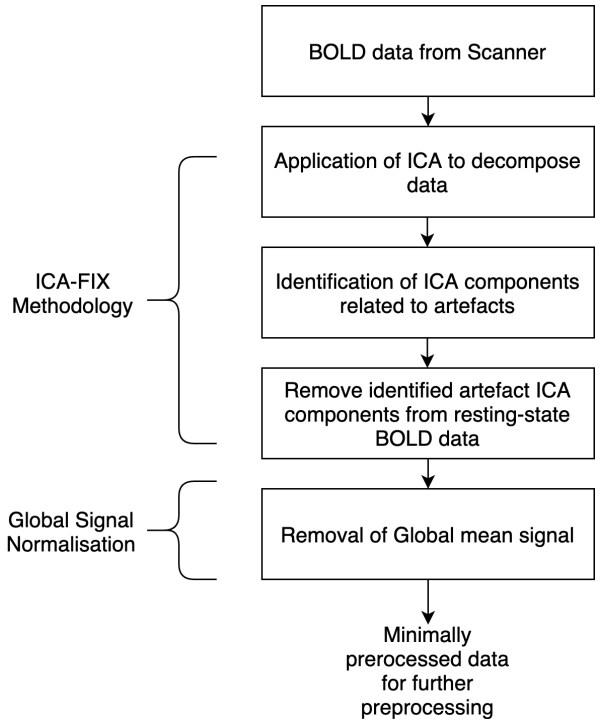

Figure 3-3: Preprocessing pipeline used at the University of Pennsylvania on rs-fMRI data obtained from HCP.

where μ is the mean of the process Z_t, ε_t is the independent and identically distributed (i.i.d.) noise with mean zero and bounded variance. In particular, the noise can be assumed to be white gaussian noise, which is described by a normal distribution with zero mean and variance σ_ε^2, denoted by $\varepsilon_t \sim WN\left(0, \sigma_\varepsilon^2\right)$. Additionally, $(1-B)^d$ is the difference operator as defined in Equation 2-15, $d \in \mathbb{R}_+$ is the *fractional-order* difference parameter, B is the backshift operator. Furthermore, $\phi(B)$ and $\psi(B)$ are the autoregressive and moving average operators defined in Equation 2-8 and 2-9, respectively.

The proposed ARFIMA (p, d, q) (model-based) filtering as shown in the block diagram in Figure 3-4, can be divided into two parts: *(i)* estimation of the fractional difference, autoregressive and moving average parameters of the filter by modelling the time series as in Equation 3-1 and *(ii)* use the ARFIMA model to obtain an infinite impulse response filter to filter out any potential noise present in the data.

- Estimation of the fractional difference parameter, d: There are numerous methods available in the literature for the estimation of d as noted in Section 2-2-3. However, Liu *et al.* in their study [29] remarks that the estimated value of d varies with the type of method used. Therefore, in this study, a grid search approach is used for the estimation of fractional difference parameter d such that the fractional differencing achieves short-term memory property and yields stationary time series. Specifically, the resting-state BOLD time series, Z_t^i, is fractionally differenced for different values of d in the range $[0.1, 5.0]$ and the number of statistically significant lags (i.e., the lags for which autocorrelation value lies outside the range $\pm 2/\sqrt{N}$, where N is the number of sample

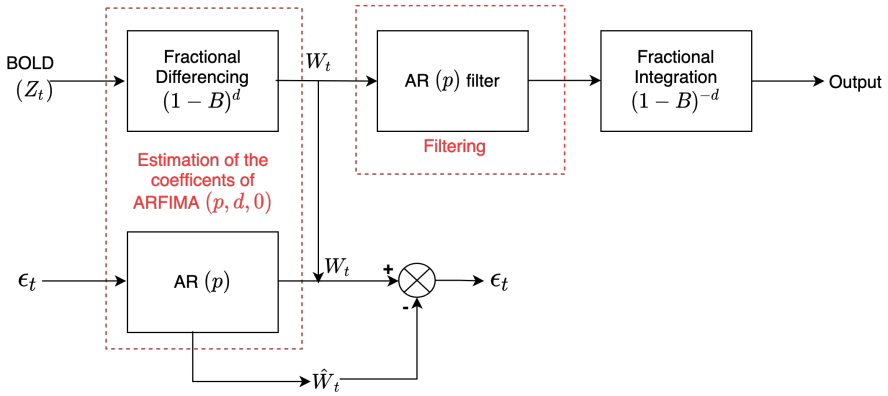

Figure 3-4: Proposed ARFIMA (p, d, q) (model-based) filtering procedure of the minimally preprocessed resting-state BOLD signal.

points) are calculated. The final value of d considered is that for which the number of statistically significant lags is minimum.

Notice that the fractional differencing of a time series yields

$$\begin{aligned}(1-B)^d Z_t &= \left(\sum_{k=0}^{\infty} \frac{\Gamma(k-d)}{\Gamma(k+1)\Gamma(-d)} B^k\right) Z_t \\ &= \left(1 - \mathrm{d}B + \mathrm{d}(d-1)B^2/2! - \cdots\right) Z_t \\ &= Z_t - dZ_{t-1} + d(d-1)Z_{t-2}/2! - \cdots .\end{aligned} \tag{3-2}$$

As such, this fractional differencing operation has an infinite impulse response; specifically, it models an infinite order autoregressive process whose parameters are defined by the fractional differencing weights. Figure 3-5 shows the value of fractional differencing weights $f(k)$ converging to 0 as $k \to \infty$ for two different values of d. Therefore, for the practical implementation, this infinite impulse response process is converted to finite impulse response by limiting the number of weights (i.e., by truncating the series). Specifically, the study truncates the series of the fractional difference weights when their absolute value is less than 1×10^{-04}.

As the ARMA models assume that the time series is stationary [47]. Therefore, after fractionally differencing the time series, the study inspects that indeed the differentiated resting-state BOLD data with the selected parameter d is stationary using the Kwiatowksi, Phillips, Schmidt and Shin (KPSS) test [67]. It tests the null hypothesis that the observed time series is stationary around a deterministic trend (for a significance level of $p < 0.05$).

- Estimation of the autoregressive parameters, p and ϕ of ARMA $(p, 0)$ model: After obtaining the fractionally differenced short-memory and stationary series, W_t, the next step is to model this time series using Autoregressive Moving Average (ARMA) (p, q) model. In order to devise a causal filter [47], the moving average parameter q is set to 0 in the ARMA (p, q) model. Therefore, the obtained fractionally differenced time series is modelled using an ARMA $(p, 0)$ process.

  Due to the inherent existence of an infinite order autoregressive process in the fractional differencing operation in ARFIMA $(p, d, 0)$ modelling, the order p of the autoregressive

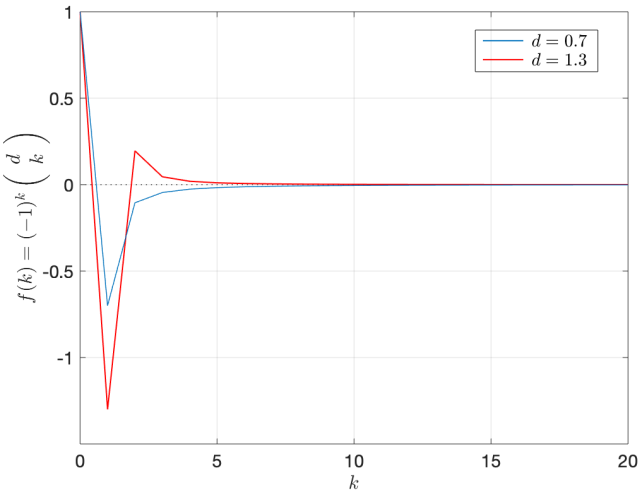

Figure 3-5: Convergence of fractional differencing weights to 0 for different values of fractional differencing parameter: $d = 0.7$ (cyan colored curve) and $d = 1.3$ (red colored curve).

component is limited to 1. This helps in restricting the number of degrees of freedom and obtaining a stable model as the weights of AR (p) serve as a scaling factor of the differentiated BOLD.

Additionally, in order to check that indeed AR (1) process is capable of capturing the dynamics of the fractionally differenced stationary time series, W_t, we start by fitting an AR model of order 1. The coefficient (ϕ) of this model is estimated using maximum likelihood principle [47] and the residual between W_t and the simulated time series $\hat{W}_t$ (Figure 3-4) from the fitted model are observed. If the residual error is statistically indistinguishable from white noise (i.e., having flat power spectrum and uncorrelated residuals), then it suggests that there is no need for higher-order fitting; otherwise, order p is increased, and then residuals are tested again [68]. The statistical significance of the residual error following a normal distribution is tested using student's t -test [69] (at a significance level of 0.05). In this study, the residuals behaved as standard white noise sequence for an AR (1) model.

- ARMA $(1, 0)$ filtering: Finally, after the estimation of filter coefficients, the fractionally differenced BOLD time series W_t is filtered through the designed ARMA $(1, 0)$ filter or AR (1) filter.

As the obtained dataset consists of data from 98 subjects in four different runs and the brain of each subject is parcellated into $n(= 100)$ ROIs, therefore, the discussed procedure is repeated for the resting-state BOLD time series of each of the ROIs for each subject across all runs. Thus, this procedure can be termed as *univariate ARFIMA* $(1, d, 0)$ *(model-based) filtering of the resting-state BOLD signal* as shown in Figure 3-6.

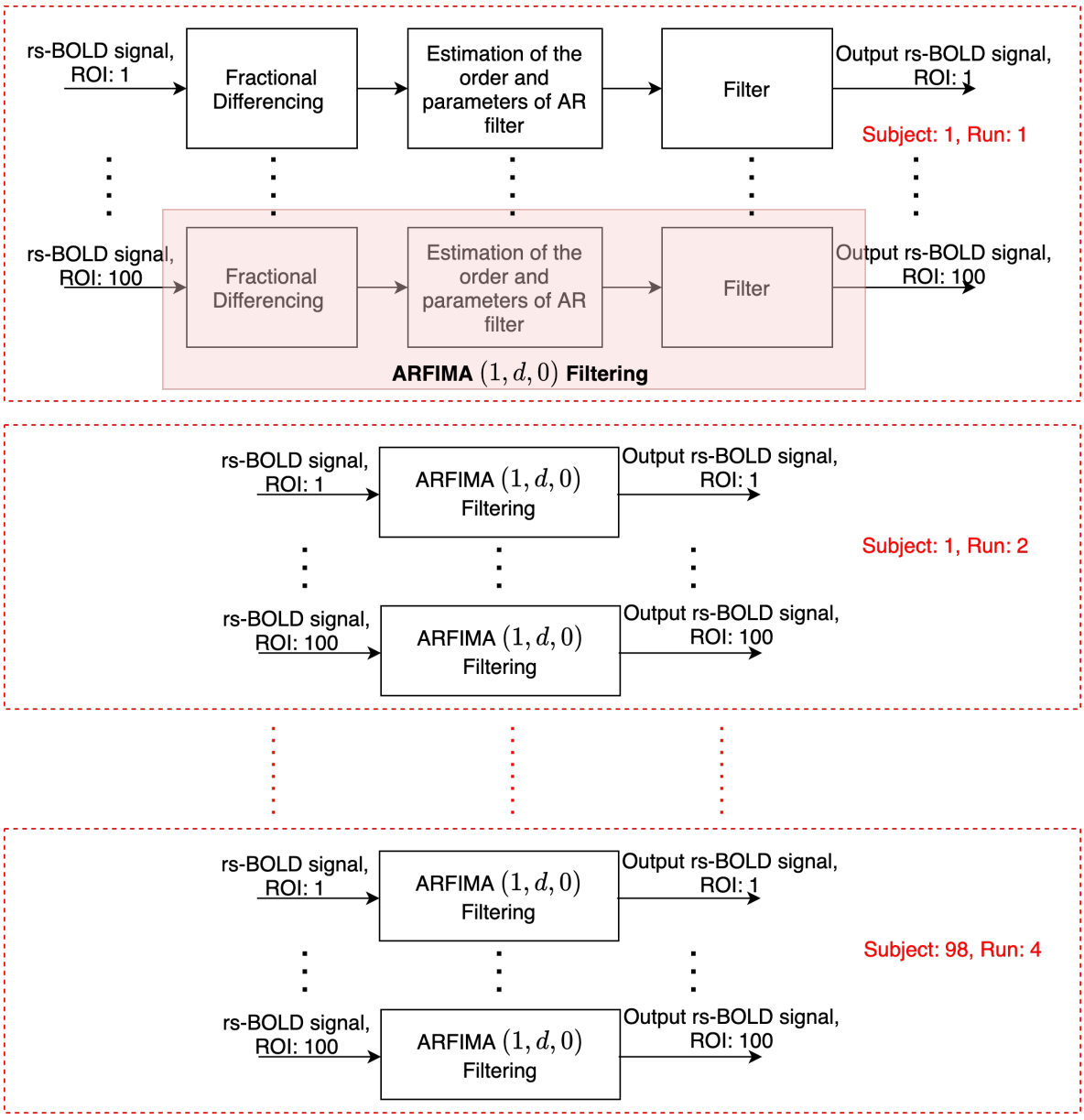

Figure 3-6: Univariate ARFIMA $(1, d, 0)$ (model-based) filtering of the minimally preprocessed resting-state BOLD (rs-BOLD) signals of 98 subjects across 4 runs. In each case, the data is aquired from 100 ROIs of the brain.

3-3 Evaluation Measures

In order to validate the impact of the proposed ARFIMA $(1, d, 0)$ filter on the resting-state BOLD data, following evaluation measures are considered.

3-3-1 Normalised power spectrum

The frequency-domain characteristics of the resting-state BOLD signal have gained huge scientific popularity [70], [71] as they have been associated with various physiological processes [72] and the resulting brain-network measures [73]. The spectral content helps to better analyse the fluctuations in BOLD due to neural activity [74]. Therefore, a normalised power spectrum is used as one of the evaluation measures to observe the effect of the proposed methodology on the resting-state BOLD signals.

Power spectrum describes the distribution of power in different frequencies present in the signal. Its formula is given by

$$P(f) = \frac{1}{N} \left| Z_t^i(f) \right|^2, \tag{3-3}$$

where $Z_t^i(f)$ is the fast fourier transform of a time series Z_t^i corresponding to the resting-state BOLD signal from ith ROI. The evaluation is performed by visual observation of the power spectrum of this signal before filtering and after the implementation of the proposed ARFIMA $(1, d, 0)$ filter. To better visualise the results, the power spectrum is normalised in its amplitude by dividing the power with the maximum power present in the signal. Therefore, normalised power spectrum

$$\Delta |P(f|) = \frac{P(f)}{max\left(|P(f)|\right)}, \tag{3-4}$$

is used for the analysis. For quantification, a statistical test (Kolmogorov–Smirnov test [75]) to test the similarity of the power spectrum of the resting-state BOLD signal and ARFIMA filtered time series is performed.

3-3-2 Functional connectivity measures

The connectivity of the brain, in general, is described as the interaction between different regions of the brain. Most conventionally, functional connectivity (FC) is defined as the temporal co-activation in the measured brain signals between two ROIs. The notion of FC, is not limited to, but has been used for the characterisation of neural bases in healthy population and also for the detection of various neurodegenerative (e.g. Alzheimer's, dementia [76], [77]), psychiatric (e.g. depression, schizophrenia [78], [79]) and neurological (e.g. stroke, epilesy [80], [81]) brain diseases. Since the fluctuations in BOLD signal can be confounded due to factors other than neuronal activity, henceforth, their effect can be carry forwarded in the FC measures as well [73]. Therefore, the results of two FC matrices based on the Pearson's correlation and coherence are compared before and after proposed filtering.

For any subject, the resting-state BOLD time series are extracted from $n\,(= 100)$ ROIs. The pairwise FC between each of the ROI gives a symmetric functional connectivity matrix of size $n \times n$ for one subject in one run. Thus, with the considered dataset for each FC measure two

matrices, one $n \times n$ matrix from the preprocessed resting-state BOLD signals and another $n \times n$ matrix from the ARFIMA $(1, d, 0)$ filtered BOLD time series are obtained. The difference matrix between both the obtained matrices (before and after filtering) gives the difference between the pairwise FC of the ROIs. The following defines the two FC measures: Pearson's correlation and coherence, used for this study.

Pearson's correlation

Pearson's correlation is a time-domain similarity measure and provides a relative measure of the linear association between two signals. It is defined by

$$\rho_{\text{corr}}\,(X,Y) = \frac{\text{cov}(X,Y)}{\sqrt{\text{var}(X)\,\text{var}(Y)}} = \frac{(X-\bar{X})(Y-\bar{Y})^T}{\left(\sqrt{(X-\bar{X})(X-\bar{X})^T}\right)\left\{\sqrt{\left((Y-\bar{Y})(Y-\bar{Y})^T\right)}\right\}}, \tag{3-5}$$

where $\text{cov}(X,Y)$ is the covariance between the signals, $\text{var}(X)$ and $\text{var}(Y)$ is the variance of signal X and Y respectively and $\bar{X}$ and $\bar{Y}$ represent the mean of the respective signals.

The Pearson correlation coefficient ρ_{corr} is scale-invariant and lies in the range from $+1$ to -1. A value closer to 0 implies no linear correlation between two signals. A positive value indicates a positive correlation, that is, both the time series signals tend to be simultaneously greater than their respective means. A negative value implies a negative correlation, that is, the time series tend to fall on opposite sides of their respective means.

Coherence

The spectral coherence, also known as *magnitude-squared coherence* assess the correlation between two signals in the frequency domain. It provides a measure of similarity between two signals at each frequency and is given by

$$\rho_{\text{coherence}}\,(X,Y) = \frac{|P_{XY}(f)|^2}{P_{XX}(f)P_{YY}(f)}, \tag{3-6}$$

where $P_{XX}(f)$ and $P_{YY}(f)$ are the respective power spectral densities of the two signals and $P_{XY}(f)$ is the cross power spectral density between the two time series. The value of the coherence $\rho_{\text{coherence}} \in [0,1]$, where 0 indicates no coherence and the value 1 strong coherence between the two time series. Since the coherence is calculated as a correlation between two signals at each frequency, the mean value of the coherence vector thus obtained can be used for further analysis.

3-3-3 Eigenmode analysis

The linear time-invariant (LTI) description (Equation 3-7) of the dynamics of system can be used to study its dynamical properties using a so-called *eigenmode decomposition* approach [82]. The model dynamics can be obtained by fitting a stochastic time series model to the observations of the system. Let $Z(k) \in \mathbb{R}^n$ be the vector of $n(= 100)$ resting-state

BOLD signals, where the ith entry, $Z_i(k)$, correspond to the resting-state BOLD signal collected at the ith ROI at the sampling time $k = 1, \ldots, t$. The dataset used for the study is acquired at $t = 1200$ sample points. Specifically, Z_k reprsented as $Z[k] = [Z_1[k] \ldots Z_n[k]]^\top$, with $k = 1, \ldots, 1200$ is the state of the system describing the evolution of the BOLD signal across different regions of brain. Therefore, the systems's state can be modelled as

$$Z(k) = AZ(k-1) + \varepsilon(k), \quad k = 1, \ldots, t, \tag{3-7}$$

where A is an $n \times n$ real matrix describing the autonomous dynamics of the system, whose elements are obtained by fitting a multivariate autoregressive model by solving a least square optimisation problem [83], and $\varepsilon(k) \in \mathbb{R}^n$ is the approximation error.

The eigendecomposition of A provides n eigenmodes, that is, the n eigenvalue-eigenvector pairs (each pair represented as : λ_i, v_i). These eigenmodes capture the spatiotemporal characteristics of the process. Specifically, each eigenvector represents an independent pattern of co-active brain regions and its corresponding eigenvalue describes the oscillation frequency of the activation pattern. The representation of eigenvalue, (λ_i) in its polar coordinates $(\theta_i, |\lambda_i|)$ provides the spatial frequency of the oscillation by

$$f_i = \frac{\theta_i}{2\pi}\delta t, \tag{3-8}$$

where δt corresponds to the sampling frequency. The frequency dictates how fast or slow the signal varies between its peaks. On the other hand, the absolute magnitude of the eigenvalue provides the stability of the signals in the regions indicated by the associated eigenvectors. Specifically, the low value of stability implies the dynamical signal will vanish in a short period of time, whereas if it gets closer to one, then it will oscillate continuously. Altogether, it is apparent that a combination of regions has a superposition of the dynamical activities captured by the combination of stability and frequency.

In this study, n eigenvalue-eigenvector pairs are obtained for each run and for each of the 98 subjects in the HCP dataset. Specifically, the $98 \times 4 \times 100 = 39200$ eigenvectors obtained across all subjects and all runs are clustered into $k = 5$ clusters using k-means clustering [84]. Similarly, the 39200 output eigenvectors corresponding to the ARFIMA filtered resting-state BOLD time series across all subjects, and all runs are clustered into 5 clusters. The cluster centroid for each cluster before and after filtering is plotted on the brain overlays (also known as "eigenbrains"), and visual inspections are performed to observe any differences in the activation patterns of different brain regions. A non-parametric statistical testing (two-sample Kolmogorov–Smirnov test [75]) is utilised to study the variations/similarity in spatial content.

Similarly, the corresponding eigenvalues are grouped based on the eigenvector's similarity and the corresponding distribution of frequency and stability (obtained from corresponding eigenvalues distribution) in each cluster is compared using statistical testing (two-sample student's t-test [69] and Wilcoxon rank sum test [85]) before and after filtering to observe variations in the spectral content.

The proposed methodology is implemented on the dataset, and its results and their analysis based on the discussed evaluation measures is given in the next chapter. An overview on the statistical tests used in this study is presented in Appendix B.

Chapter 4

Results and Discussion

This chapter consists of the results obtained from the implementation of the proposed method to model the dynamics of resting-state BOLD data. All the results have been obtained in MATLAB®(9.7, R2019b). In order to demonstrate the utility of the proposed approach, first the method is tested with a synthetic BOLD signal which has properties similar to the resting-state BOLD signal (e.g., long-term memory [24], [25], [26] and higher power in lower frequencies [1], [86], [87] as captured by the sACF and power spectrum, respectively), to which white noise is added. Afterwards, the designed fractional filter is applied to the original resting-state BOLD dataset, and its utility is tested using the evaluation measures discussed in Chapter 3.

4-1 Synthetic BOLD signal

One of the major challenge for the evaluation of the filtering method on the resting-state BOLD signal is the lack of clean signal that includes fluctuation only due to neural activity of the brain. Thus, the study begins with the implementation of the proposed ARFIMA $(1, d, 0)$ filtering on a principled synthetic signal such that the "ground-truth" signal is known. The oscillations in resting-state BOLD signals are generally considered and observed to be low frequency oscillations in the range of $\sim 0.01 - 0.15$ Hz [1], [71], [86], [87] and are observed to have long-memory dependency [24], [25], [26]. Therefore, the synthetic BOLD signal is generated as a sum of sinusoidal signals of different frequencies to obtain a signal with long-term memory property and specific power spectrum, mathematically represented as

$$X_t = \sum_{i=1}^{N} A_i \sin\left(2\pi f_i t\right) \tag{4-1}$$

where X_t is the synthetic signal, A_i and f_i is the amplitude and frequency of the ith signal, respectively, and N is the number of signals. For the purpose, a vector of 10 random frequencies in the range $0.1 - 0.15$ Hz was generated to mimic the presence of the low-frequency

fluctuations in the resting-state BOLD signals. Additionally, the synthetic signal was sampled at 1.3889 Hz in order to emulate the sampling frequency of resting-state BOLD signal of the HCP dataset. Figure 4-1a shows the presence of low-frequency fluctuations in the range $0.1 - 0.15$ Hz in the power spectrum of the simulated BOLD signal and Figure 4-1b depicts the presence of long-memory property through the inverse power law behaviour of the sample autocorrelation plot.

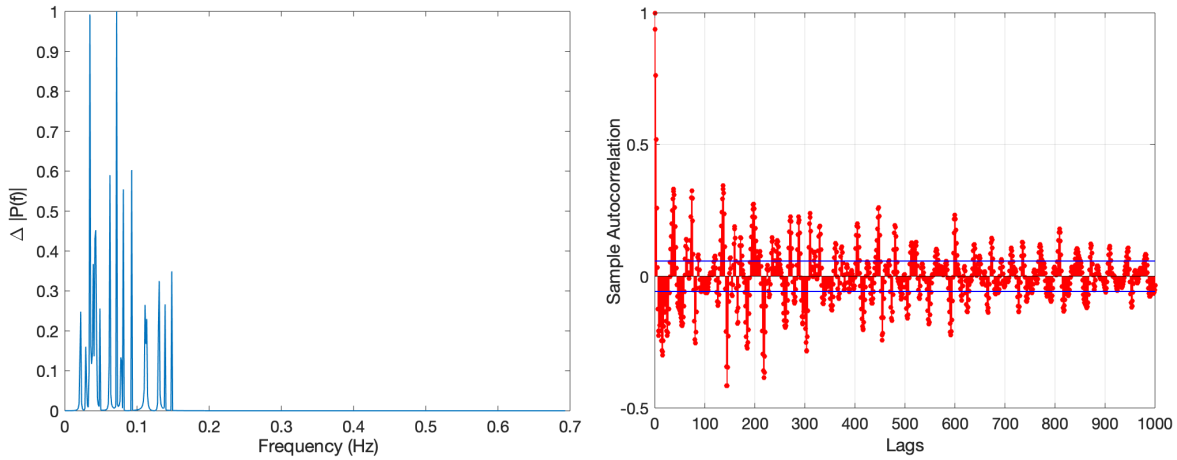

(a) Normalised power spectrum consisting of low frequency fluctuations.

(b) Slowly decaying sampled ACF plot depicting the presence of long-memory property in the signal.

Figure 4-1: Properties of the simulated synthetic BOLD signal.

The simulated BOLD signal was artificially corrupted with the two different white gaussian noise sequences, $\varepsilon_t \sim WN(0, 10)$ and $WN(0, 100)$. Afterwards, the noisy synthetic signal underwent proposed ARFIMA $(1, d, 0)$ filtering to filter out the artificial noise injected into the signal. The value of d for the ARFIMA $(1, d, 0)$ filtering of the synthetic signal with noise variance 10 and 100 was obtained using the procedure described in Section 3-2. Figure 4-2 shows that the value of d for which the number of statistically significant lags are minimum in: *(a)* synthetic signal with noise variance 10 is 3.8, and *(b)* signal with variance of noise 100 is 2.6, respectively. Additionally, the exponentially declining autocorrelation plot of the fractionally differenced synthetic signal in Figure 4-3 illustrates the modelling of the long-memory property for both noise variances. Visual inspection of the normalised power spectrum in Figure 4-4 and 4-5 shows that the proposed ARFIMA $(1, 3.8, 0)$ and ARFIMA $(1, 2.6, 0)$ filter, respectively, is able to cancel the effect of high frequency noise added to the clean ground-truth signal (as can also be seen in the zoomed in version of these plots in higher frequency region).

Several other synthetic signals were created using the described procedure, and similar results were obtained with others as well. Figure A-1 and A-2 shows the effect of proposed filtering on two other synthetic signals. Thus, the proposed denoising procedure was capable of retrieving the ground-truth signal from different artificial noise-induced synthetic BOLD signals.

After the success of the proposed methodology in removing white noise from synthetic BOLD signal, this section presents the result of the implementation of the proposed approach on resting-state BOLD signals from the HCP dataset.

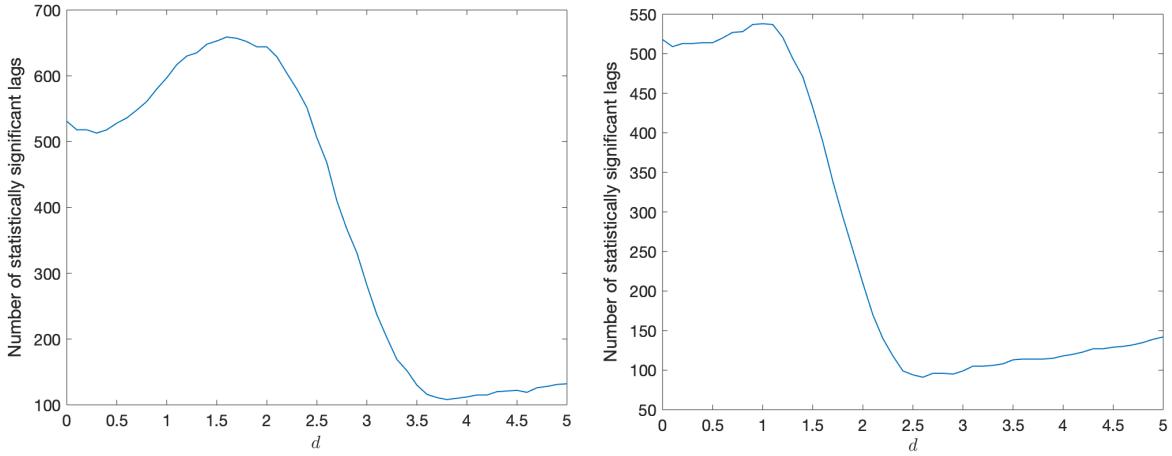

(a) **(b)**

Figure 4-2: Variation in the number of statistically significant lags in the sampled ACF of fractionally differenced noise-induced synthetic BOLD signal with different values of fractional differencing parameter d. (a-b) shows the variation in d for the synthetic signal corrupted with white noise, $\varepsilon_t \sim WN(0, 10)$ and $\varepsilon_t \sim WN(0, 100)$, respectively. For the signal in (a) the value of d was selected as 3.8 and in (b) it was selected as 2.6.

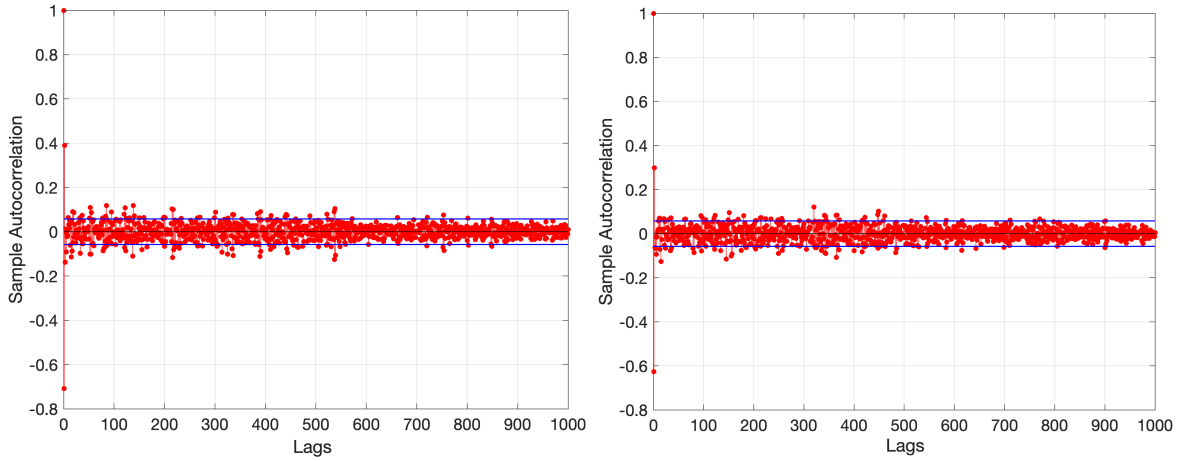

(a) **(b)**

Figure 4-3: Exponentially decaying sample autocorrelation plot of of the fractionally differenced simulated artificially noise induced synthetic signal, $\varepsilon_t \sim WN(0, 10)$ and fractional difference parameter, $d = 3.8$ in (a), and $\varepsilon_t \sim WN(0, 100)$ and $d = 2.6$ in (b).

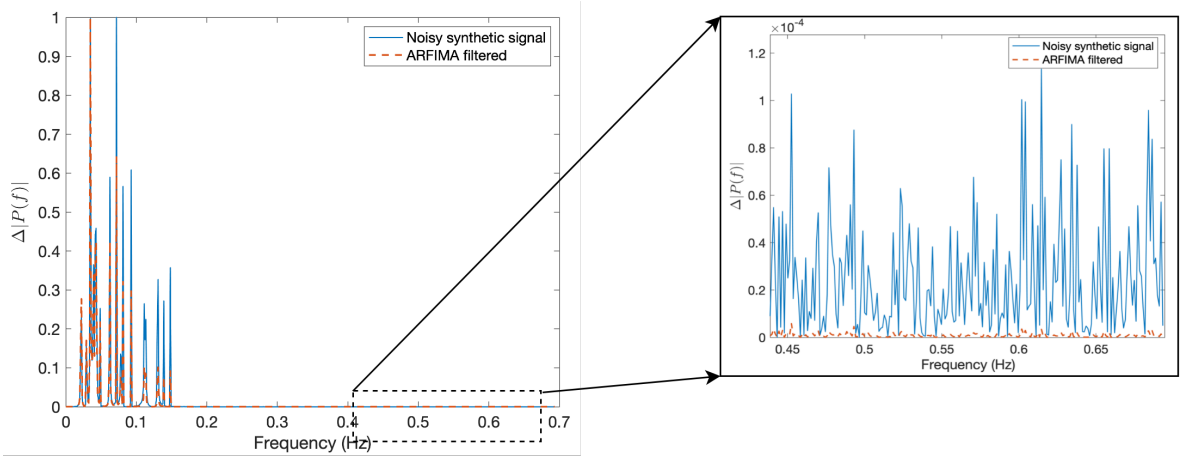

Figure 4-4: Comparison of the normalised power spectrum plot of the noisy synthetic BOLD signal (cyan colored curve, $\varepsilon_t \sim WN\,(0, 10)$) and ARFIMA $(1, 3.8, 0)$ filtered synthetic BOLD signal (dashed orange). The box in the right panel depicts the power spectrum zoomed-in at the higher frequency region.

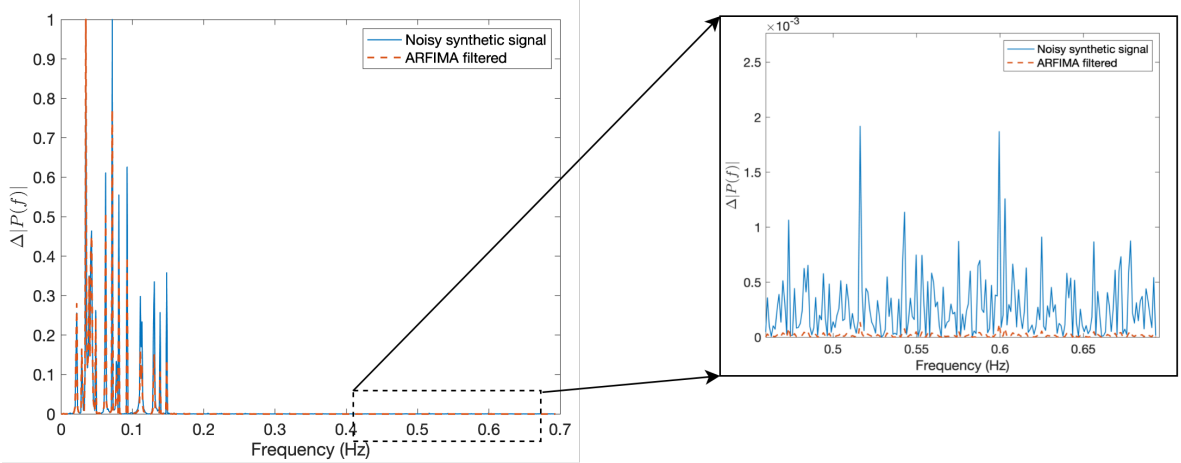

Figure 4-5: Comparison of the normalised power spectrum plot of the noisy synthetic BOLD signal (cyan colored curve, $\varepsilon_t \sim WN\,(0, 100)$) and ARFIMA $(1, 2.6, 0)$ filtered synthetic BOLD signal (dashed orange). The box in the right panel depicts the power spectrum zoomed-in at the higher frequency region.

4-2 ARFIMA filtering of the acquired resting-state BOLD signals

Subsequently, the same proposed ARFIMA methodology was implemented with the resting-state BOLD signals from the dataset. Both the subject level and group level analysis to illustrate the effect of the proposed methodology on the resting-state BOLD data acquired from the 98 subjects in four runs are presented in this section. The fractional difference parameter d and the autoregressive parameter ϕ of the ARFIMA $(1, d, 0)$ is estimated using the procedure described in Section 3-2 for each time series acquired from $n\,(= 100)$ regions of interest (ROIs) of each subject across all runs individually. Hence, in this procedure, the value of fractional difference parameter d and AR coefficient ϕ varies for each BOLD time series.

For instance, the value of d was estimated as $0.7, 0.3$ and 0.5 for ROIs $7, 11$ and 37, respectively, of subject 1, run 1 and $0.6, 0.1$ and 0.1 for the same ROIs of the subject 3, run 2. Table 4-1 shows the mean value of d for $n\,(= 100)$ ROIs averaged across all subjects in all runs. Besides, the value of AR (1) parameter was obtained as $-0.1007, 0.0034, -0.1548$ and -0.1379 for ROIs $1, 7, 11$ and 98, respectively of subject 1, run 1, thus, providing evidence that the parameters are different for different ROIs. Similarly, the values of the AR (1) parameters for the same regions of subject 3, run 1, are $-0.0992, -0.1820, 0.0406$ and -0.0301 ; thus, providing evidence that these are different across subjects. Fig 4-6 shows the mean of the estimated values of the AR (1) parameter, ϕ across different ROIs. Thus, implying that the proposed ARFIMA $(1, d, 0)$ filtering approach is deployed channel-wise. Additionally, Kruskal-Wallis test [88] on both parameters ϕ and d showed that the mean between these parameters for different subjects and different runs was significantly different (at a significance level of 0.05).

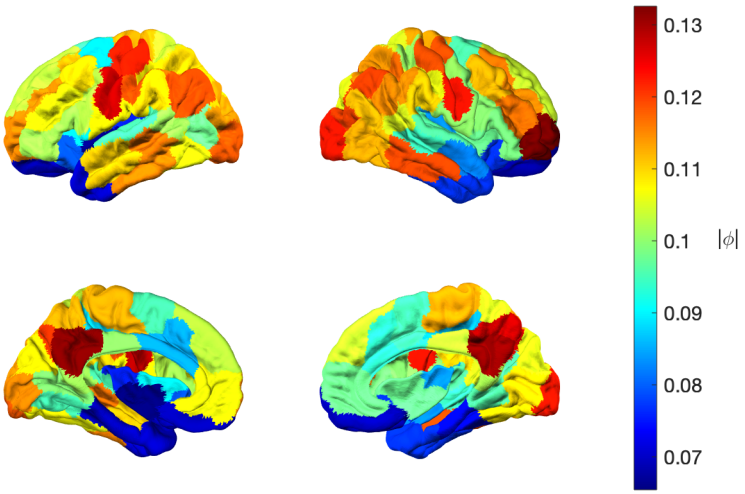

Figure 4-6: Mean value of the absolute AR(1) parameter averaged across the ROIs of all 98 subjects across all 4 runs.

Table 4-1: Mean value of the fractional difference parameter $'d'$ averaged across the ROIs of all 98 subjects in all 4 runs (i.e., 98×4).

ROIs	d (Mean ± std. deviation)	ROIs	d (Mean ± std. deviation)	ROIs	d (Mean ± std. deviation)	ROIs	d (Mean ± std. deviation)
1	0.6679 ± 0.1779	26	0.6566 ± 0.1636	51	0.6051 ± 0.1860	76	0.6849 ± 0.1396
2	0.9617 ± 0.1751	27	0.3702 ± 0.1398	52	0.9411 ± 0.1770	77	0.4186 ± 0.1269
3	0.7202 ± 0.2031	28	0.1946 ± 0.1036	53	0.9130 ± 0.1762	78	0.1880 ± 0.0980
4	0.9416 ± 0.1769	29	0.2464 ± 0.1112	54	0.7268 ± 0.2078	79	0.2292 ± 0.1200
5	0.5003 ± 0.1811	30	0.4533 ± 0.1769	55	0.4906 ± 0.1643	80	0.7051 ± 0.1501
6	0.5191 ± 0.1796	31	0.8339 ± 0.1467	56	0.8758 ± 0.1753	81	0.6849 ± 0.1500
7	0.7643 ± 0.1936	32	0.7163 ± 0.1451	57	0.4406 ± 0.1344	82	0.6003 ± 0.1437
8	0.7209 ± 0.1926	33	0.6227 ± 0.1436	58	0.6865 ± 0.1809	83	0.6967 ± 0.1691
9	0.6110 ± 0.1782	34	0.5980 ± 0.1502	59	0.4722 ± 0.1642	84	0.9449 ± 0.1646
10	0.5097 ± 0.1778	35	0.7921 ± 0.1466	60	0.6158 ± 0.1790	85	0.7056 ± 0.1501
11	0.2804 ± 0.1293	36	0.6031 ± 0.1508	61	0.4934 ± 0.1772	86	0.7140 ± 0.1655
12	0.5640 ± 0.1562	37	0.3344 ± 0.1371	62	0.3161 ± 0.1343	87	0.3158 ± 0.1285
13	0.7452 ± 0.1917	38	0.6421 ± 0.1441	63	0.5069 ± 0.1516	88	0.7212 ± 0.1320
14	0.6209 ± 0.1615	39	0.7008 ± 0.1496	64	0.7457 ± 0.1732	89	0.8622 ± 0.1764
15	0.6370 ± 0.1719	40	0.6306 ± 0.1481	65	0.7110 ± 0.1711	90	0.6770 ± 0.1477
16	0.7791 ± 0.1689	41	0.6306 ± 0.1716	66	0.6541 ± 0.1658	91	0.6599 ± 0.1425
17	0.6969 ± 0.1779	42	0.6719 ± 0.1578	67	0.7821 ± 0.1678	92	0.5258 ± 0.1444
18	0.5747 ± 0.1651	43	0.9824 ± 0.1789	68	0.6648 ± 0.1723	93	0.7344 ± 0.1601
19	0.5714 ± 0.1709	44	0.8013 ± 0.1789	69	0.6084 ± 0.1615	94	0.3426 ± 0.1427
20	0.5347 ± 0.1485	45	0.6819 ± 0.1537	70	0.5227 ± 0.1531	95	0.6395 ± 0.1733
21	0.6875 ± 0.1536	46	0.3482 ± 0.1529	71	0.7712 ± 0.1670	96	0.4566 ± 0.1344
22	0.2370 ± 0.1408	47	0.7358 ± 0.1775	72	0.4531 ± 0.1301	97	0.2566 ± 0.1188
23	0.4365 ± 0.1363	48	0.4526 ± 0.1259	73	0.3495 ± 0.1186	98	0.3880 ± 0.1505
24	0.3495 ± 0.1317	49	0.2503 ± 0.1807	74	0.4622 ± 0.1551	99	0.5635 ± 0.1582
25	0.4561 ± 0.1528	50	0.5658 ± 0.1637	75	0.8531 ± 0.1610	100	0.5685 ± 0.1727

4-2-1 Normalised power spectrum

The comparison of the power spectrum of the resting-state BOLD signals before and after filtering shows that the proposed filtering often leads to changes that seem to affect mainly the high-frequency components. In order to show the spatial disparity in the power spectrum the results of the proposed ARFIMA $(1, d, 0)$ filtering on three different ROIs are presented in Figure 4-7. The value of d was estimated to be $0.7, 0.3$ and 0.5 as illustrated in Figure 4-8. The three shown power spectrums are such that they have different characteristics in terms of the presence of power in the frequency region. Specifically, Figure 4-7a depicts the effect of filtering on the normalised power spectrum of ROI: 7 (present in the visual peripheral network of the brain), which has maximum power at lower frequencies. In contrast, Figure 4-7b shows the effect of filtering on the normalised power spectrum of ROI: 11 which lies in the somatomotor network with power spread out over the whole of its frequency range, and Figure 4-7c corresponds to the ROI: 37 lying in the executive control network and has most of the power in its lower frequencies but still consists of a significant amount of power in the higher frequency region. Thus, depicting a behaviour similar to a low-pass filter.

Additionally, the statistical similarity of the normalised power spectrum of each ROI before and after filtering, using two-sample Kolmogorov–Smirnov test [75] at a significance level of 0.05 was tested. The statistical comparison between the normalised power spectrum of each of the ROI of all the subjects across all runs before and after proposed filtering indicates that of all the power spectrum corresponding to total $98 \times 4 \times 100 = 39200$ resting-state BOLD signals, around 51% (i.e., 19966 signals) were statistically distinguishable. Thus, indicating the impact of proposed filtering on the frequency content of the signal.

Comparison between the low-pass filter and the derived ARFIMA filter

Despite depicting a behaviour similar to a low-pass filter, the difference between the characteristics of an LPF (first-order butterworth) and the proposed ARFIMA filter was observed. For instance, Fig 4-9a displays the difference between the magnitude bode plot of an LPF (first-order butterworth) with a cut off frequency of 0.1Hz and the proposed ARFIMA $(1, 0.3, 0)$ filter for the BOLD signal corresponding to ROI: 11 lying in the somatomotor auditory region of the brain. Upon using both the filters, it can be observed from Fig 4-9b that the LPF eliminates the higher frequencies. However, the derived filter does not eradicate rather attenuates the high-frequency component thus, preserving some of the high-frequency information that may be relevant to the neural activity. The attenuation of the order of around 50dB at higher frequencies in case of low-pass Butterworth filter and of around 6dB with the derived ARFIMA $(1, 0.3, 0)$ filter explains the observed behaviour. Hence, it provides evidence that the derived filter has some characteristics different from the ordinary LPF.

Furthermore, because the ARFIMA model-based approach is a time-domain method, various other scenarios are expected. Specifically, for most signals, ARFIMA filtering performs attenuation at higher frequencies, as can be seen in Fig 4-7. Still, sensitivity in some frequency distributions was noticed, where a small amount of amplification was observed in the higher frequencies. The amplification was witnessed in around 17.5% of the entire resting-state time series, filtered using the proposed filter. For instance, Figure 4-10a shows one such ROI where the high-frequency components are actually amplified. The amount of amplification can be

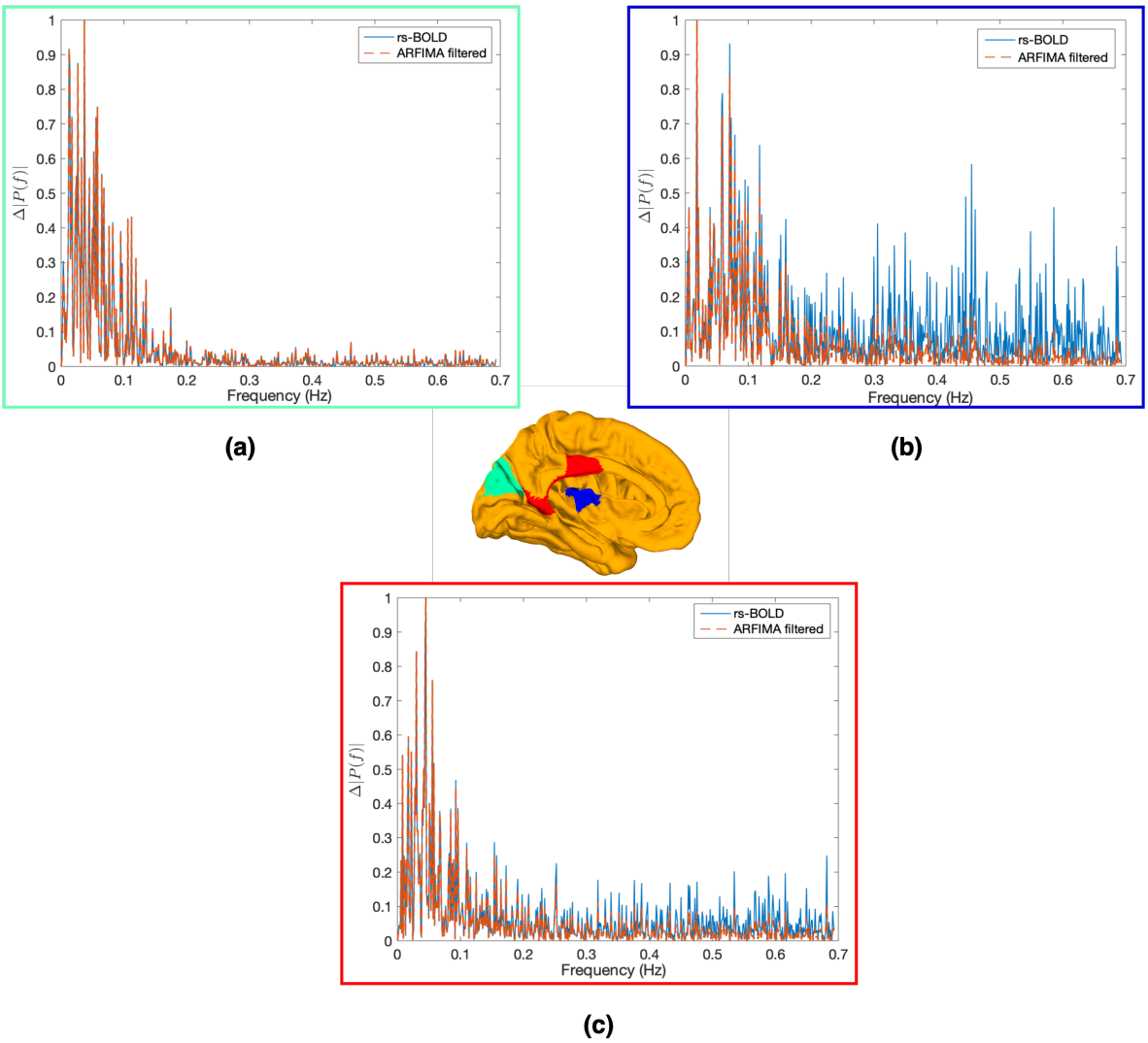

Figure 4-7: Comparison of the normalised power spectrum plot of the preprocessed (cyan-colored curve) and ARFIMA $(1, d, 0)$ filtered (dashed orange curve) resting-state BOLD (rs-BOLD) signal for three different ROIs. The location of each of the three ROI is presented in the brain overlay (in the centre) in different colours. The power spectrum of the corresponding ROI is outlined in the same colored box. (a) illustrates the impact of proposed ARFIMA $(1, 0.7, 0)$ filtering on the ROI: 7 (green colored region) lying in the visual peripheral brain network. (b) shows the effect of proposed ARFIMA $(1, 0.3, 0)$ filtering on the ROI: 11 (blue colored region) in the somatomotor auditory network of the brain. (c) depicts the impact of proposed ARFIMA $(1, 0.5, 0)$ filtering on the ROI: 37 (red colored region) in the executive control brain network.

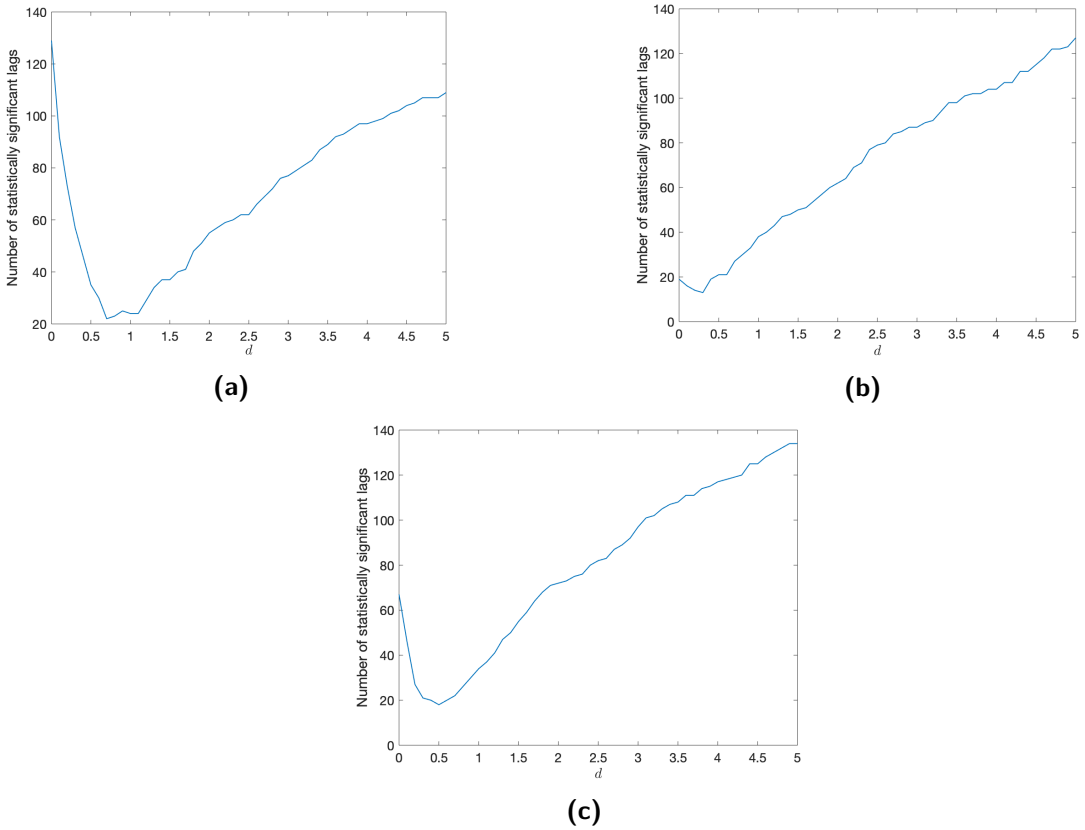

Figure 4-8: Variation in the number of statistically significant lags in the sampled ACF with changing value of d of resting-state BOLD signals from three different ROIs of one of the subject. (a) ROI: 7 lying in the central visual brain network. (b) ROI: 11 in the somatomotor auditory network of the brain. (c) ROI: 37 in the executive control network. The value of d was selected to be $0.7, 0.3$ and 0.5 for ROIs in (a), (b), and (c), respectively

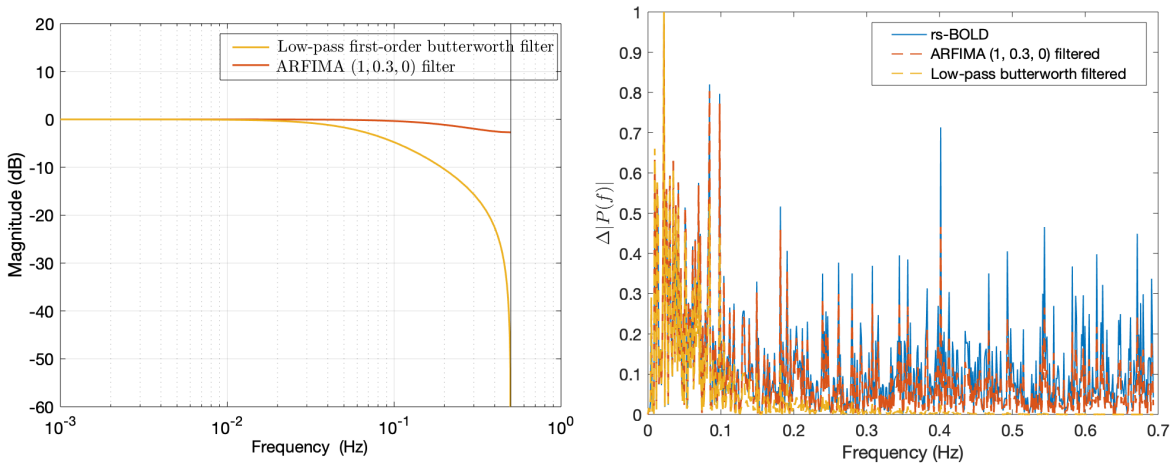

(a) (b)

Figure 4-9: Difference between the characteristics of a LPF and the proposed ARFIMA filter. (a) Magnitude Bode plot of the transfer function of the LPF (first-order butterworth filter) with cut off frequency: 0.1Hz (yellow curve) and the derived ARFIMA $(1, 0.3, 0)$ filter (orange curve) for ROI: 11 corresponding to the somatomotor auditory region of the brain. (b) Comparison of the normalised power spectrum of the rs-BOLD (cyan colored), first-order butterworth filtered (dashed yellow) and ARFIMA $(1, 0.3, 0)$ filtered (dashed orange) BOLD signal of ROI: 11.

observed in the magnitude bode plot of the proposed filter in Figure 4-10b, which is of the order of 0.1 dB. This provides evidence of the versatility of the proposed filtering scheme which is tailored for each of the channels and the associated data under consideration. Although we lack the ground-truth of these signals, the synthetic examples explored provide converging evidence that the proposed filters are attaining their objective.

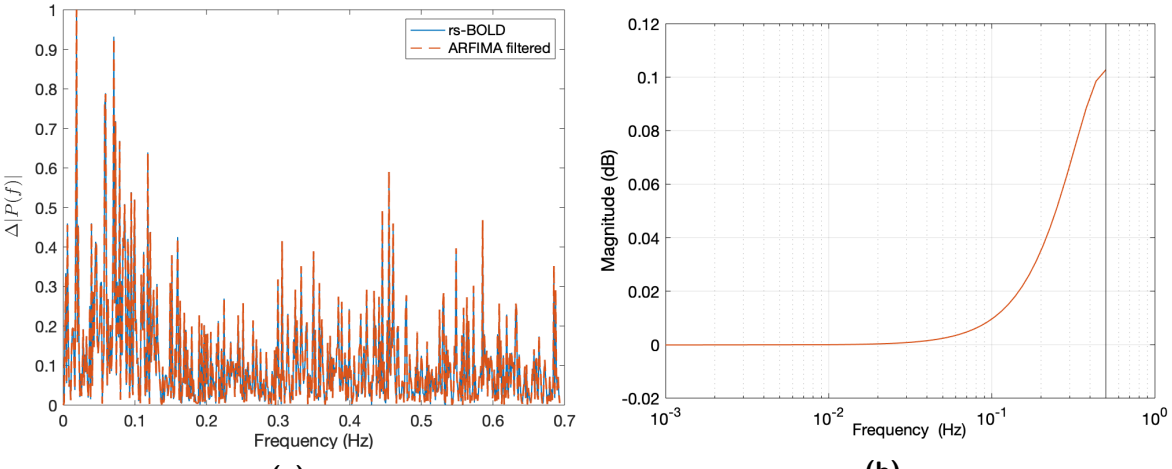

(a) (b)

Figure 4-10: Amplification in the high frequencies for one of the ROI. (a) shows the normalised power spectrum of the rs-BOLD signal (cyan curve) and the ARFIMA filtered signal (dashed orange curve) for one of the ROI. (b) Magnitude bode plot of the derived ARFIMA $(1, 0.2, 0)$ filter (for the ROI shown in (a)) depicting amplification in higher frequencies.

The primitive studies denote that the fluctuations due to neural activity in resting-state BOLD signals are associated with the low-frequencies [11], [89], [90], however, technical advances in the MR imaging techniques led to the identification of resting-state networks in frequencies higher than 0.1Hz [70], [91], [92]. The latter suggests that the high-frequency fluctuations in resting-state BOLD signals are not only the result of artefacts but also include the contribution from underlying neuronal activity. Therefore, completely filtering out the high-frequency components do not seem to be an ideal denoising approach. Thus, it is remarkable to highlight that the proposed filter seems to attenuate/amplify the higher frequencies when required.

4-2-2 Functional Connectivity analysis

Functional connectivity FC matrices (based on Pearson's correlation and coherence) between each ROI of the brain for each subject across all runs are found individually in both the cases with the resting-state BOLD signals and ARFIMA $(1, d, 0)$ filtered BOLD signals. To perform the group-level analysis, the FC matrices obtained from each subject in each run are averaged, and one representative FC matrix in terms of mean $\pm$ standard deviation is considered. Since FC is dominated by the high power in slow frequencies; therefore, these measures capture the slow-frequency properties of the signal. As it was observed from the power spectrum analysis that the effect of filtering seems to be more heavily present at the high-frequency component of the signal, hence, the FC matrix may not observe any significant changes due to filtering. Figure 4-11 depicts the representative FC matrix before and after filtering found based on Pearson's Correlation. Similarly, Figure 4-12 shows the FC matrix based on coherence. The difference mean FC matrices in both cases (Figure 4-11c and 4-12c) indeed depict that the mean FC matrices before and after filtering are similar. Additionally, the two-sample Kolmogorov–Smirnov test [75] on the pre and post-filtered mean FC matrices failed to reject the null hypothesis that they are statistically indistinguishable (at a significance level of 0.05).

4-2-3 Eigenmode analysis

The dynamics in the resting-state BOLD signals can be modelled by the linear time-invariant system approximation [82], [93]. The system, thus, obtained can be decomposed into its so-called eigenmodes. Eigenmodes (represented by corresponding eigenvalue-eigenvector pairs) can be used to capture the spatiotemporal characteristics of the process. The underlying system is approximated from the resting-state BOLD signals as well from the ARFIMA filtered signals. Further, eigenvectors from all the subjects before and after filtering are computed and clustered into $k = 5$ clusters using k-means clustering [84] to capture the resting state networks [93] (for an overview of resting-state networks, see Appendix C). The spatial correlation shown in Fig 4-13 between the identified cluster centroid (through clustering of eigenvectors before and after filtering) and the seven resting-state networks (RSNs): visual (Vis) network, somatomotor (SM) network, dorsal attention network (DN), ventral attention network (VN), limbic network, executive control network (ECN) and default mode network (DMN) identified in [2] reveals that each cluster consists of one or more RSNs and the contribution of each RSN in each cluster (before and after filtering) remains the same.

Specifically, the eigenmode decomposition and clustering helps to: *(a)* reveal the heterogeneous spatial profile of the eigenmodes of the brain and *(b)* to leverage these now teased out

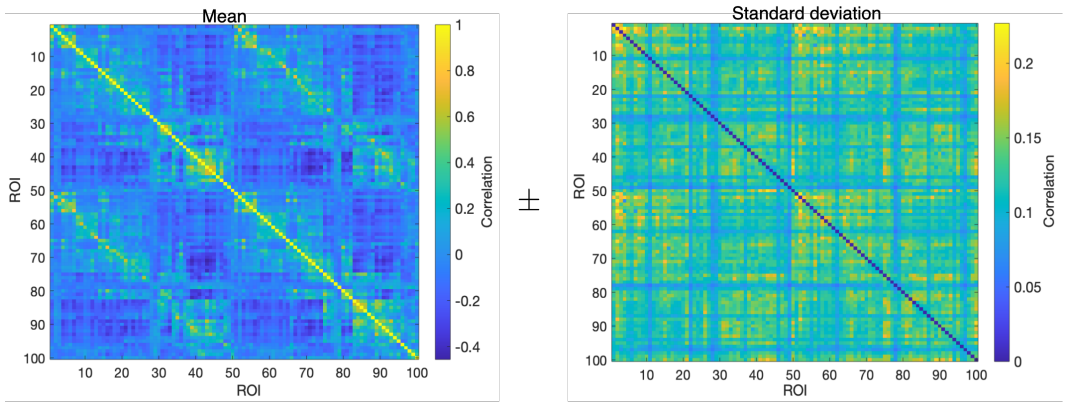

(a)

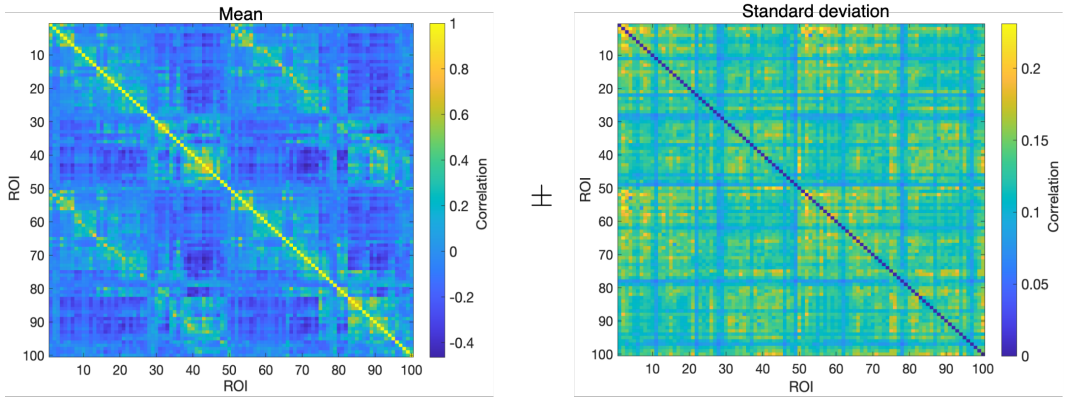

(b)

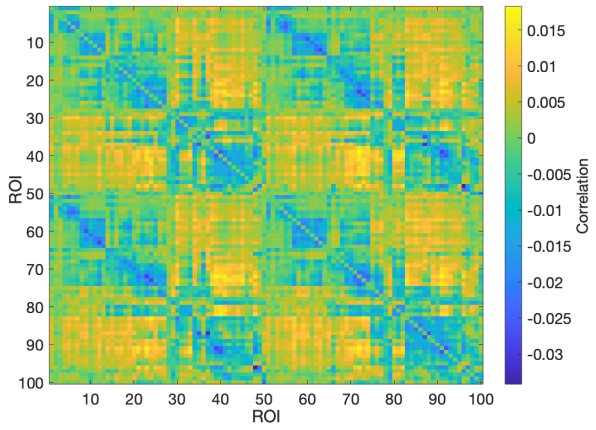

(c)

Figure 4-11: Whole brain FC matrix (comprising of 100 ROI) defined based on Pearson's Correlation. The Pearson's Correlation FC matrix of each subject in each run is averaged across to find one representative FC matrix (mean $\pm$ std. deviation). (a) Pearson's correlation matrix (mean $\pm$ std. deviation) (for 100 ROI) obtained from the resting-state BOLD dataset. (b) Pearson's correlation matrix (mean $\pm$ std. deviation) (for 100 ROI) obtained from the ARFIMA $(1, d, 0)$ filtered resting-state BOLD signals. (c) The difference between the mean Pearson's correlation matrix of the preprocessed dataset (a) and the filtered resting-state BOLD time series of the whole brain (b).

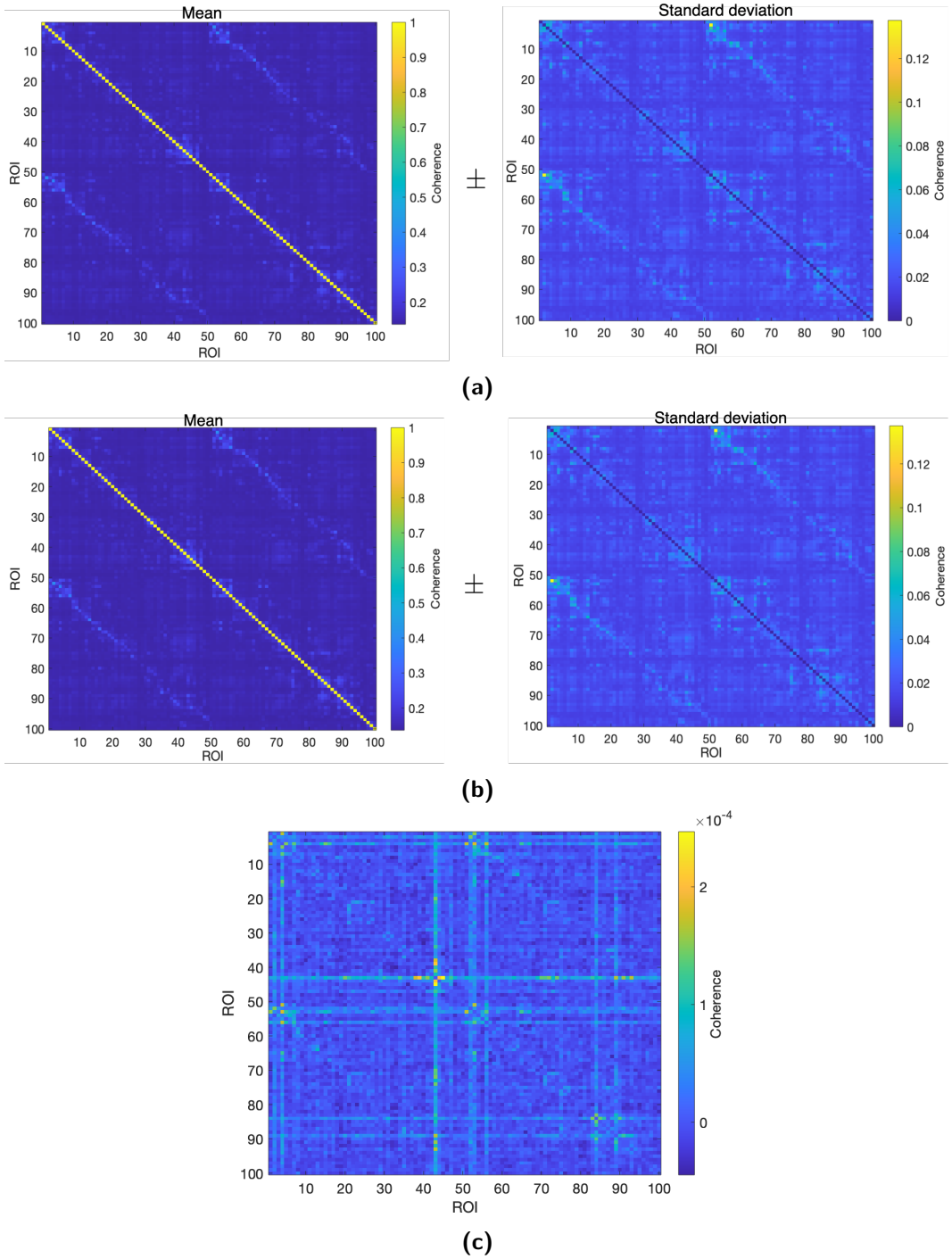

Figure 4-12: Whole brain FC matrix (comprising of 100 ROI) defined based on coherence. The FC matrix of each subject in each run is averaged across to find one representative FC matrix (mean $\pm$ std. deviation). (a) Coherence FC matrix (mean $\pm$ std. deviation) (for 100 ROI) obtained from the resting-state BOLD time series. (b) Coherence FC matrix (mean $\pm$ std. deviation) (for 100 ROI) obtained from the ARFIMA $(1, d, 0)$ filtered resting-state BOLD signals. (c) The difference between the mean coherence FC matrix of the resting-state BOLD dataset (a) and the ARFIMA filtered time series of the whole brain (b).

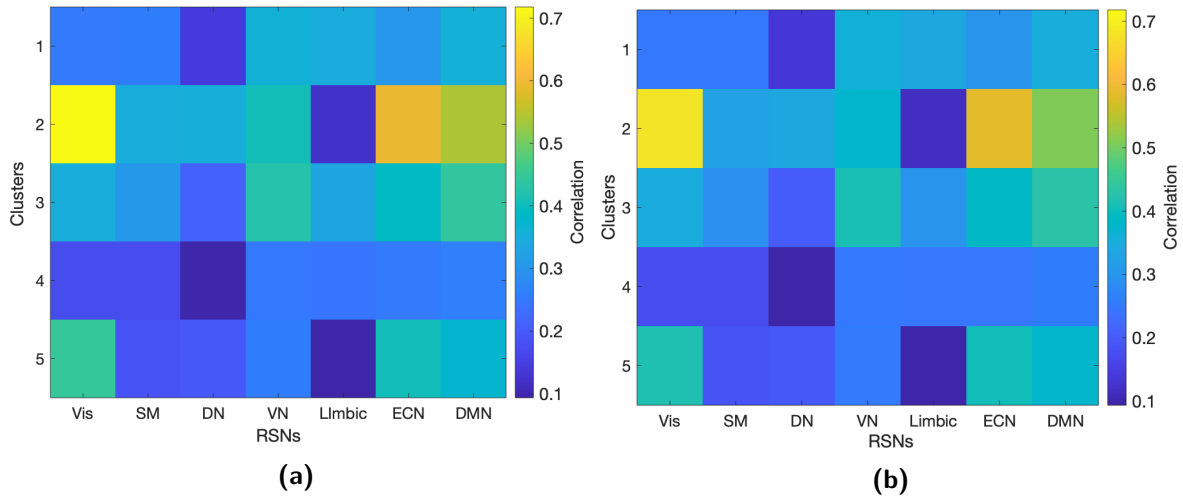

Figure 4-13: Similarity between centroid of the clusters and RSNs. (A-B) denotes the spatial correlation between clusters and resting state networks before and after ARFIMA filtering on the resting-state BOLD data, respectively.

clusters (i.e., the clusters formed from the eigenvectors of the system from ARFIMA filtered signals) to better localize any changes after filtering (that potentially impacted some RSNs differently [possibly due to their intrinsic spectral profile]).

Fig 4-14 shows the 5 cluster centroids (obtained from k-means clustering on the associated eigenvectors of the resting-state BOLD signals) in the left panel and the cluster centroids (obtained from k-means clustering on the associated eigenvectors corresponding to ARFIMA $(1, d, 0)$ filtered BOLD signals) in the right panel, plotted on the brain overlays (also known as "eigen brains"). The cluster centroids were normalised by subtracting each centroid by its minimum element. In the figure, the larger the value in a given region defined by an arbitrary unit (AU), larger is the involvement of that region in the underlying dynamics at any given time. The nomenclature used in this study is as follows: the eigen brains in Figure 4-14 inside blue colored box correspond to cluster 1, cluster 2 is outlined in orange colored box, cluster 3 in yellow outline, cluster 4 in purple colored box and cluster 5 in green colored outlined box.

Visual comparison of the so-formed 5 clusters in Figure 4-14 reveal that cluster 1 to 4 (in blue, orange, yellow and purple boxes, respectively) looks identical. However, some changes in the visual and default mode RSNs in cluster 5 (green box) can be observed. Additionally, the two-sample Kolmogorov–Smirnov test [75] was used to test the statistical similarity between the eigenvector cluster centroid of the respective cluster before and after clustering at a significance level of 0.05. The test results failed to reject the null hypothesis that the corresponding eigenvector cluster centroid before and after filtering are significantly similar.

Nonetheless, the result of the implementation of the proposed filter on the temporal dynamics of the system is observed by witnessing the variation in the spectral content given by the associated eigenvalues of the resting-state and ARFIMA filtered BOLD signals. The top and the bottom central plot of Figure 4-14 shows the distribution of the eigenvalues (frequency vs stability) before and after ARFIMA $(1, d, 0)$ filtering, respectively. The two-sample student's t-test [69] and Wilcoxon rank sum test [85] between the distribution of frequency (given

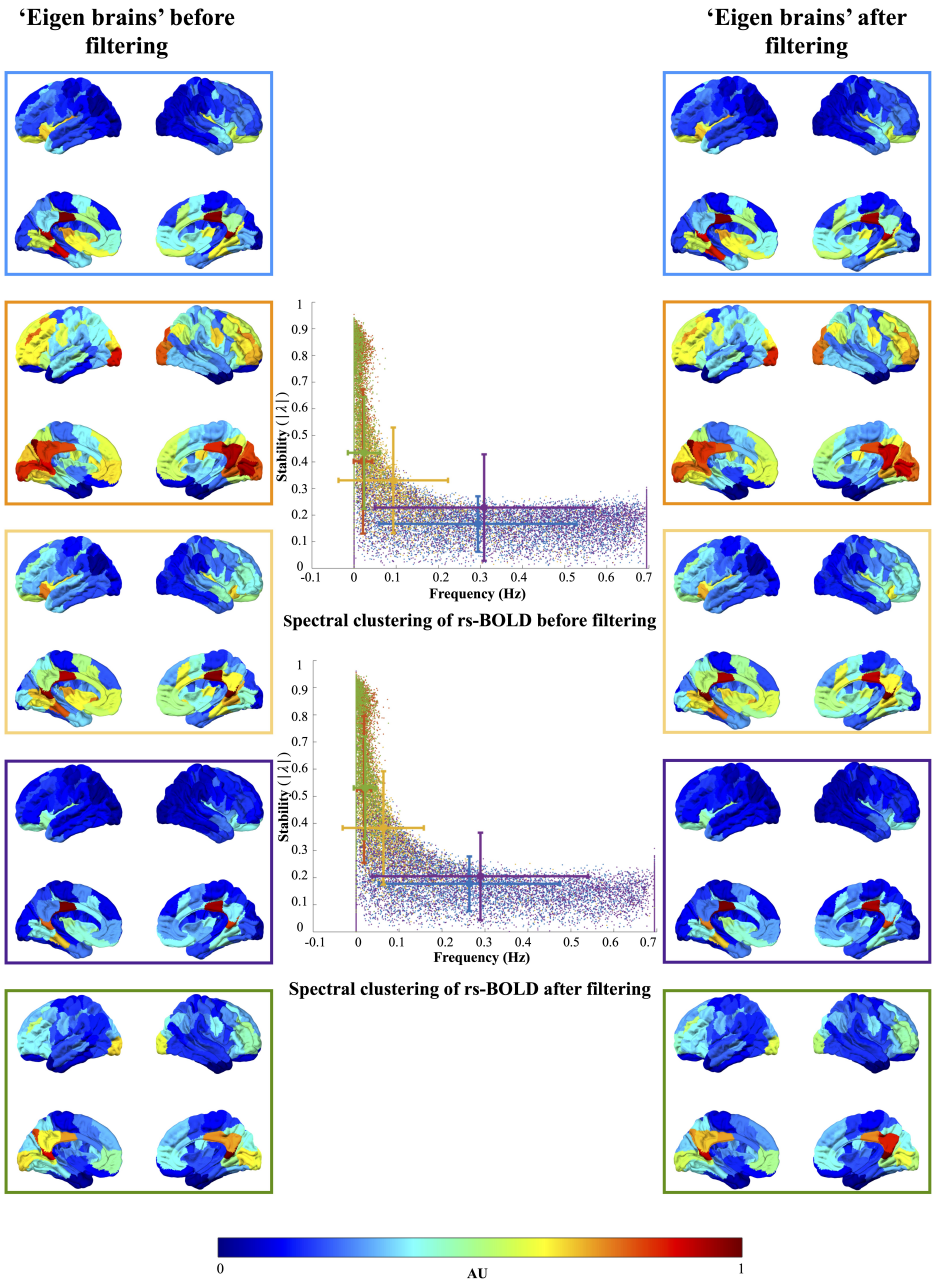

Figure 4-14: Clustering of eigenvectors and eigenvalues obtained from resting-state BOLD signal and ARFIMA $(1, d, 0)$ (model-based) filtered signals. All eigenvectors from all subjects were normalised and clustered into 5 clusters using k-means clustering. The clusters were color-coded across all subjects and all runs (98 subjects $\times$ 4 runs $\times$ 100 ROIs $=$ 39,200 eigenvalues). The color codes blue, orange, yellow, purple and green correspond to cluster $1, 2, 3, 4$ and 5, respectively. The central plot shows the distribution of eigenvalues based on the frequency (the argument of eigenvalue) and stability (the absolute magnitude of eigenvalue) of resting-state and ARFIMA filtered BOLD signals. Error bars represent the mean and standard deviation of the average stability and frequency of each cluster. The eigenvalues are color coded based on the five identified clusters. The brain overlays in the left and right panel represent the spatial distribution of the eigenvector cluster centroid of resting-state BOLD signals before and after filtering, respectively. Colorbar represents the normalised values of cluster centroid for each cluster (left and right panel).

Table 4-2: Comparison of the mean stability (magnitude of eigenvalue) and mean frequency (argument of eigenvalue) of the identified clusters from the resting-state BOLD dataset (before filtering) and ARFIMA filtered resting-state BOLD signals (after filtering).

	Mean frequency (mean ± std. deviation)		Mean stability (mean ± std. deviation)	
	Before filtering	After filtering	Before filtering	After filtering
Cluster 1	0.2943 ± 0.2341	0.2637 ± 0.2112	0.1665 ± 0.1037	0.1773 ± 0.1011
Cluster 2	0.0210 ± 0.0219	0.0185 ± 0.0167	0.4015 ± 0.2713	0.5250 ± 0.2696
Cluster 3	0.0930 ± 0.1300	0.0632 ± 0.0948	0.3304 ± 0.1981	0.3832 ± 0.2093
Cluster 4	0.3090 ± 0.2598	0.2890 ± 0.2509	0.2281 ± 0.1997	0.2044 ± 0.1617
Cluster 5	0.0236 ± 0.0383	0.0209 ± 0.0262	0.4340 ± 0.2904	0.5312 ± 0.1893

by the argument of eigenvalue, Equation 3-8) before and after filtering revealed that it was statistically distinguishable for all the clusters (at a significance level of 0.05). Similarly, the pairwise student's t -test [69] and Wilcoxon rank sum test [85] on the stability (obtained from the absolute magnitude of eigenvalue) distribution of the resting-state BOLD data and the ARFIMA filtered signals showed statistical difference for all the clusters ($p < 0.05$).

Additionally, Table 4-2 compares the average value of the stability and frequency between each cluster of the eigenvalues of the preprocessed system and ARFIMA filtered system. The comparison shows that the stability of the system improves by around 7% in cluster 1, around 25% in cluster 2 and 5, and by approximately 16% in cluster 3 after implementation of the proposed filtering.

These results highlight filtering-related changes. More intriguingly, the spectral profiles associated with the clusters changes after filtering. Thus, providing additional evidence that the proposed filter modifies the (spatiotemporal) spectral content of the resting-state BOLD signals.

Chapter 5

Conclusion

The blood-oxygen-level-dependent (BOLD) signal arises from a complex interaction between neuronal activity and vascular processes. Resting-state functional magnetic resonance imaging (rs-fMRI) studies observe the changes in the fluctuations of the BOLD signals in response to the neural activity. However, the intrinsic BOLD signal fluctuations can be corrupted due to the presence of different confounds, some of which are outlined in this study. Different resting-state cleanup methods have been devised for effective confound removal. Most of these methods deal with known sources of noise. Therefore, further refinement of the existing preprocessing pipeline can help in better interpretation of resting-state fMRI data. This study, thus, proposes a method in the aforementioned direction of further cleaning of the preprocessing resting-state BOLD signals.

Having witnessed the long-memory dependency in the resting-state BOLD signals, the work proposed the use of autoregressive fractional integrative processes ARFIMA $(1, d, 0)$ for the purpose. The proposed ARFIMA (model-based) approach is univariate filtering i.e., the coefficient ϕ of the autoregressive AR (1) component and fractional differencing parameter d of the ARFIMA $(1, d, 0)$ filter are estimated for each resting-state BOLD signal individually. It is worth noticing that the approach for the estimation of fractional difference parameter d was a grid search approach such that the fractional differencing achieves short-term memory and yields stationary time series. The order of autoregressive component was limited to 1 to reduce the degrees of freedom and to obtain a stable model as their weights serve as a scaling factor of the differentiated BOLD. Additionally, we furloughed the moving average component to ensure that we deal with causal filters.

A major challenge for evaluating the denoising method of the resting-state BOLD signal is the unavailability of the ground-truth signal. Therefore, first, the proposed filter is evaluated with a principled synthetic BOLD signal which has statistical properties similar to the resting-state BOLD signal identified in the literature (i.e., long-term memory and low-frequency fluctuations [1], [24], [25], [26], [86], [87]). The proposed denoising procedure was capable of retrieving the ground-truth signal from the artificial noise-induced synthetic BOLD signal. Thus, it provides evidence that the filter is attaining its objective.

Subsequently, the proposed filter was implemented with the preprocessed resting-state BOLD signals from the HCP dataset. The dataset consists of data from 98 subjects acquired across 4 different runs. The impact of the proposed methodology was evaluated using four different evaluation measures i.e., normalised power spectrum, functional connectivity (FC) based on Pearson's correlation, FC based on coherence, and eigenmode decomposition.

Section 4-2-1 highlights the variations in the normalised power spectrum of the resting-state BOLD signals pre and post proposed ARFIMA filtering. The effect of the proposed filter was observed on the high-frequency components wherein the filter seems to attenuate/amplify the high-frequency components based on the frequency distribution of the resting-state BOLD signal. FC matrices based on both Pearson's correlation and coherence were observed to be insensitive to the differences in BOLD signals pre and post-filtering (Section 4-2-2). This is mainly due to the evidence (as observed from power spectrum analysis) that the proposed filter has dominant effects in the high frequencies, but these FC measures capture the low frequencies of the signals. However, the results from eigenmode decomposition and k- means clustering in Section 4-2-3 provided additional evidence of the filtering-related changes. Particularly, the variation in the spectral content of the system captured through the statistical differences in the distribution of frequency and stability of the LTI systems approximated from the signals before and after proposed ARFIMA filtering illustrated the said changes.

All these results suggest that the proposed methodology filtered out the data that was not consistent with the proposed model, which evidence suggests to be properly modeled by fractional-order processes and, further, corroborated by the synthetic examples explored. Thus, we conjecture that we were able to remove some additional noise that could be due to sporadic activity which could not be eliminated through data preprocessing, or maybe due to additional artefacts introduced by such preprocessing. Hence, the proposed method can be used as an additional step in the already existing preprocessing pipeline. The results also provides an evidence that the proposed scheme is suitable to model the dynamics of preprocessed resting-state BOLD signals.

5-1 Limitations

The major limitation of the study is the evaluation of the proposed denoising approach on the dataset. The unavailability of standard resting-state BOLD signal for distinguishing fluctuations due to neural component from artefacts poses a great challenge. Although, to overcome this limitation, a synthetic BOLD signal which follows the observed properties of the original BOLD signals was created. However, it is impossible to state beyond doubt that the signal being filtered out from the original resting-state BOLD signal is the noisy component or was the source of neural activity. The other limitation lies in the estimation of the fractional difference parameter, d, in the proposed ARFIMA filtering. The method utilised in this work is a grid search approach. But, selecting a value too high may lead to over differencing of the time series and thus, can introduce artificial memory [22], [50]. Therefore, a novel method can be developed to estimate d, which can also help improve the results obtained in this study.

5-2 Future work

The current research focuses on the univariate filtering of the resting-state BOLD signals, however, the spatiotemporal dependencies between different regions of interest of a brain cannot be ignored [94], [95]. Thus, future work should focus on extending the proposed filter to the multivariate domain.

Additionally, the value of fractional differencing parameter d in this study was considered constant over a period of time for resting-state BOLD time series for a particular ROI. Future research should account for possible variations, like those that occur in criticality analysis of electrocorticogram signals in epilepsy [96] patients, or critical transition phenomena found in nature [97].

Finally, in this study, static FC is considered as one of the evaluation metric, largely based on their common usage in the resting-state fMRI data analysis [98], [99]. However, recently FC has been observed to fluctuate over time [100] and has opened window to the new research area called dynamic functional connectivity (dFC) [101], [102]. Future work could observe the effect of the proposed filter on the dFC metrics.

Appendix A

Synthetic BOLD signal

This chapter presents the implementation of proposed ARFIMA filtering on two different synthetic signals, simulated as described in Section 4-1.

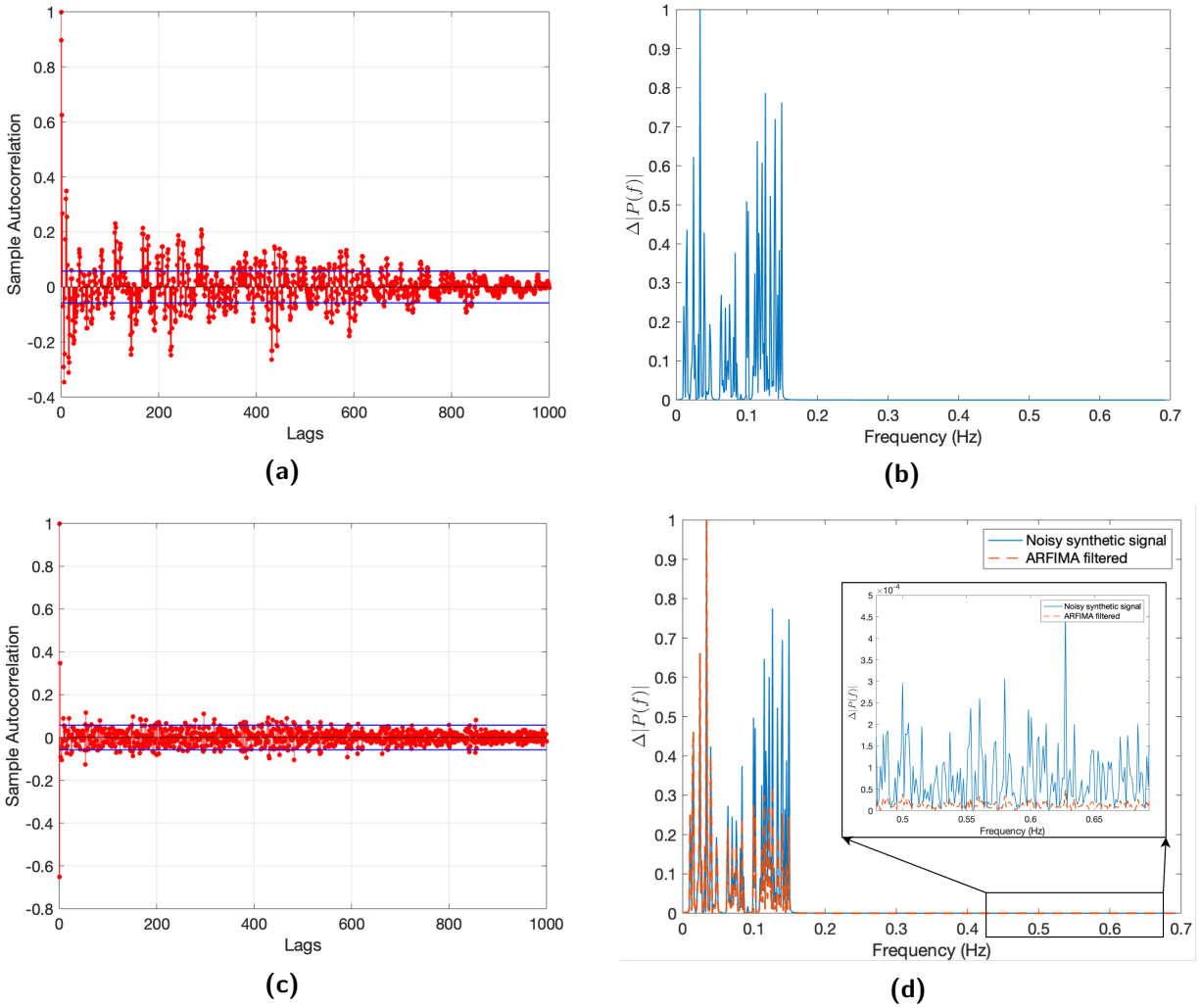

Figure A-1: Autocorrelation and normalised power spectrum plots of unfiltered and filtered synthetic BOLD signal. (a) Slowly decaying sampled ACF plot of the simulated synthetic signal. (b) The power spectrum of synthetic BOLD signal consisting of low frequency fluctuations in the range of $0.01 - 0.15$ Hz. An artificial white noise is added to the created synthetic BOLD signal. (c) shows the sampled ACF of the fractionally differenced $(d = 3.8)$ noisy synthetic BOLD signal. (d) shows the normalised power spectrum plot of unfiltered dummy BOLD signal (cyan) and the ARFIMA $(1, 3.8, 0)$ filtered BOLD signal (dashed orange) embedded with zoomed in plot at higher frequency.

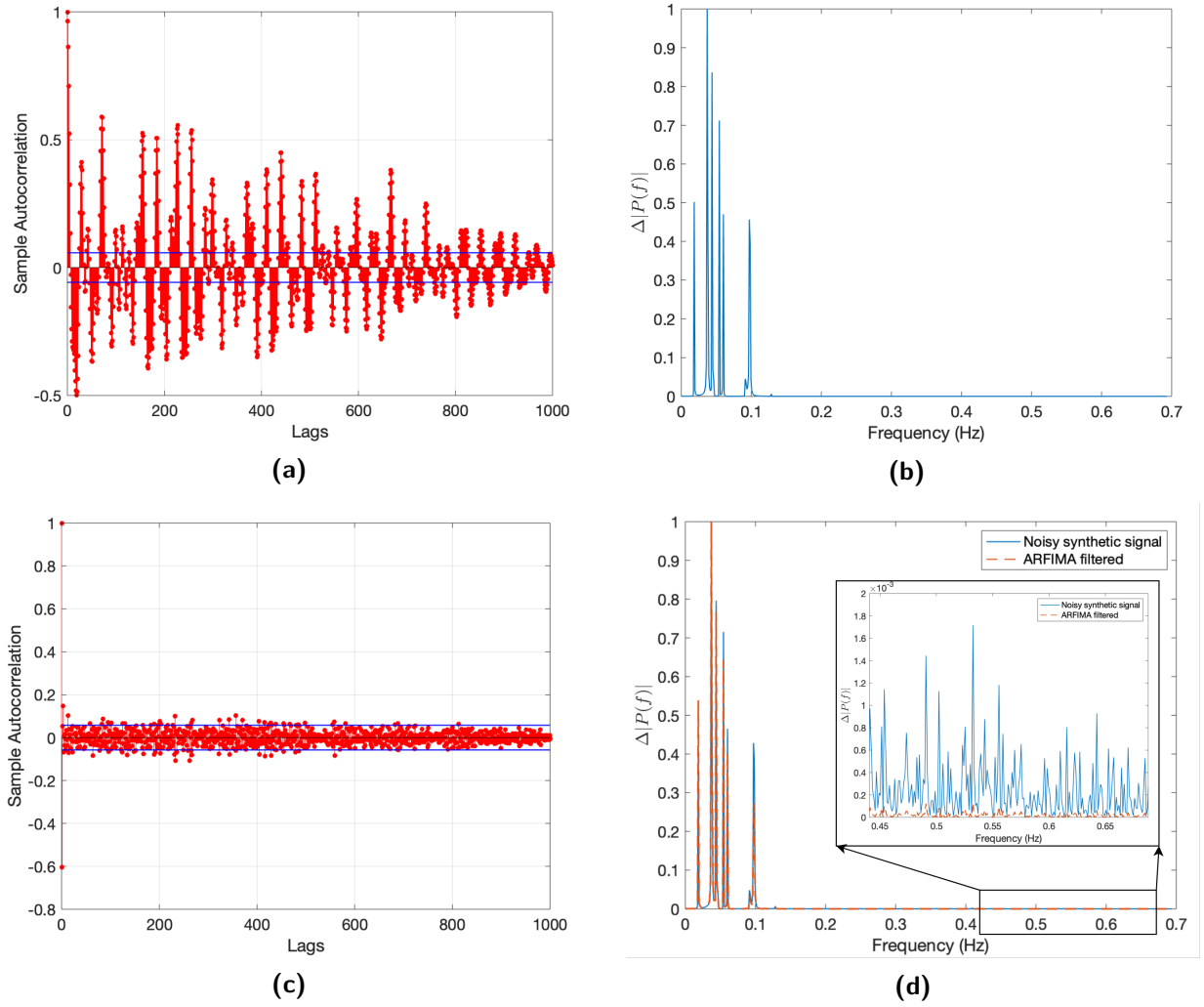

Figure A-2: Autocorrelation and normalised power spectrum plots of unfiltered and filtered synthetic BOLD signal. (a) Slowly decaying sampled ACF plot of the simulated synthetic signal. (b) The power spectrum of synthetic BOLD signal consisting of low frequency fluctuations in the range of $0.01 - 0.15$ Hz. An artificial white noise is added to the created synthetic BOLD signal. (c) shows the sampled ACF of the fractionally differenced $(d = 2.4)$ noisy synthetic BOLD signal. (d) shows the normalised power spectrum plot of unfiltered dummy BOLD signal (cyan) and the ARFIMA $(1, 2.4, 0)$ filtered BOLD signal (dashed orange) embedded with zoomed in plot at higher frequency.

Appendix B

Statistical Tests

This chapter highlights various statistical tests used in the study. It is worth emphasising that in statistical tests, the rejection of the null hypothesis implies that the alternative hypothesis is accepted within a defined significance level. However, failure of the rejection of the null hypothesis does not suggest that the null hypothesis can be accepted.

B-1 KPSS test

Kwiatowksi, Phillips, Schmidt and Shin (KPSS) [67] proposes a Lagrange-Multiplier (LM) for testing the null hypothesis that the observed time series is stationary around a deterministic trend. KPSS test considers the alternative hypothesis that the observable series has a unit root. The rejection of the null hypothesis implies that it is certain (within a defined significance level) the series has a unit root. Thus, the KPSS hypothesis test is:

H_0	:	Series is stationary
H_1	:	Unit root is present
Test Statistic	:	The test uses Lagrange multiplier test statistic to test for constant variance
α	:	Significance level (95%)

B-2 One Sample student's t- test

This statistical parametric test is used to test if the time series follows a normal distribution and is defined as [69]:

H_0	:	Vector follows a normal distribution with mean equal to 0 and unknown variance.
H_1	:	The population distribution does not have a mean equal to zero.
Test Statistic	:	$t = \frac{\bar{x}-\mu}{s/\sqrt{n}}$

where $\bar{x}$ and μ are the sample and hypothesized population mean respectively, s is the sample standard deviation, and n is the sample size.

α : Significance level (5%)

B-3 Two-sample student's t- test

The two-sample student's t- test is a parametric used to test if the data in vectors x and x comes from independent random samples from normal distributions with equal means and variance is defined as [69]:

H_0 : x and y comes from normal distribution with equal means and equal but unknown variance.

H_1 : Data in x and y comes from populations with unequal means.

Test Statistic : $t = \frac{\bar{x}-\bar{y}}{\sqrt{\frac{s_x^2}{n}+\frac{s_y^2}{m}}}$
where $\bar{x}$ and $\bar{y}$ are the sample means, s_x and s_y are the sample standard deviations, and n and m are the sample sizes.

α : Significance level (5%)

B-4 Wilcoxon rank sum test

It is a non-parametric test used to test if the two vectors x and y have the same probability distribution [85].

H_0 : Data in x and y are samples from continuous distributions with equal medians.

H_1 : Data in x and y are samples from continuous distributions with unequal medians.

Test Statistic : z-statistic.

α : Significance level (5%)

B-5 Two-sample Kolmogorov–Smirnov test

This test is used to test if the distribution of data in vectors x and y are statistically similar [75]. It is defined as:

H_0 : Data in the vectors x and y are from same continuous distribution.

H_1 : Data in the vectors x and y are from different continuous distributions.

Test Statistic : It evaluates the difference between the cummulative distribution function of the two sample data vectors over the range of x in each dataset.

α : Significance level (5%)

B-6 Kruskal-Wallis test

It is a non-parametric statistical test to determine whether data from several groups come from same distribution [88]. For the purpose, the test compares the medians of the groups of data in matrix X.

H_0	:	Samples in the columns of matrix X are drawn from populations with same distribution.
H_1	:	Atleast one column in matrix X has a different distribution.
Test Statistic	:	chi-square statistic
α	:	Significance level (1%)

Appendix C

Resting-State Networks

A network is defined as a set of objects that interact or share some relationship with one another. The objects in these networks are symbolised by *nodes* and the relationship between them by *edges* [103]. The network of brain, in this way, can be considered as a complex and an efficient network [104]. A representation of the network of brain consists of nodes as the interacting units which are identified by parcellating the brain into homogeneous and unique regions (e.g., brain areas). The connections between these regions can be anatomical (i.e., physical or structural connection) or functional (i.e, synchronous neuronal oscillations). The functional connectivity between these identified regions of interest is studied through interaction between these nodes defined by a pairwise relationship between each node (e.g., the presence of a significant correlation between two area's resting-state timecourses) [103].

A number of group resting-state studies have detected spatially separated regions in the brain whose BOLD signal fluctuations show temporal correlation during rest [11], [89], [2]. Such regions showing coherent BOLD fluctuations across time during rest constitute resting-state networks (RSNs) or intrinsic connectivity networks (ICNs). In this study, the term RSN is used.

Although depending on the methods used to study functional connectivity (e.g. ICA or seed-based analysis), or on different group of subjects, the identified RSNs may differ [105], [106], [107], [108]. However, there is a large similarity between the findings and hence, has led to the definition of seven major RSNs [109]. The identified seven major RSNs: visual (Vis) network, somatomotor (SM) network, dorsal attention network (DN), ventral attention network (VN), limbic network, frontoparietal or executive control network (ECN) and default mode network (DMN) are shown in Figure C-1.

RSNs are characterised by having a default mode of functioning reflecting their ongoing intrinsic activity [110]. The reason for the study of these networks during rs-fMRI is due to the fact that some regions that are active during rest may be deactivated during certain activities [111]. The idea of the presence of these networks in resting-state is analogous to that of a computer, implying that even in the absence of any task, the human brain has background activity.

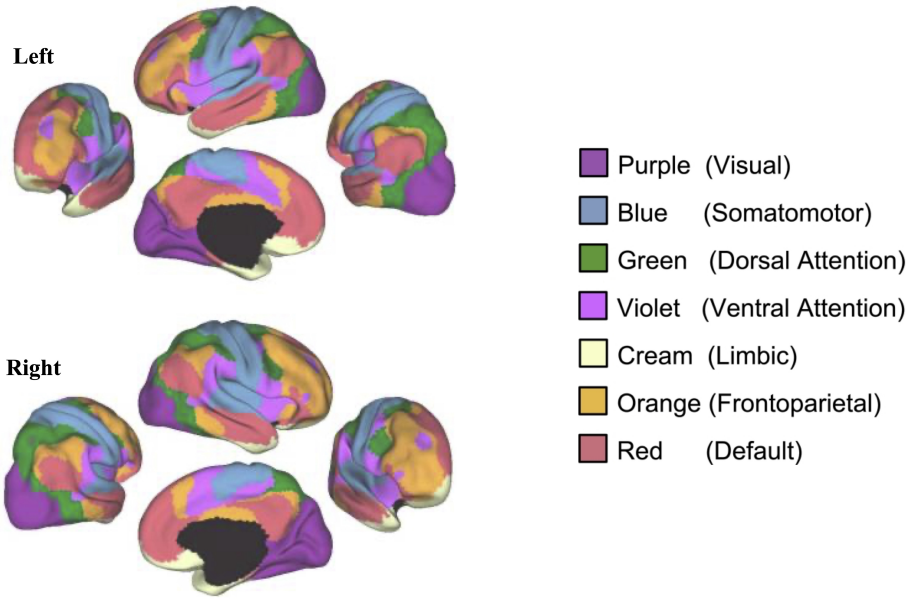

Figure C-1: Seven major identified resting-state networks in the human brain plotted on the brain overlays [2]. The networks are distinguished by the specific color codes as displayed in the legend

One of the important resting-state networks which is used for analysing neurological state is Default Mode Network (DMN). DMN is a group of brain regions consisting of precuneus and posterior cingulate, bilateral inferior–lateral–parietal and ventromedial frontal cortex [16]. The DMN is specific to the resting-state as it is characterised by reduced activity during task-based activity [112] and increased intrinsic activity during resting-state [113]. The changes in DMN have also been seen in subjects in a coma state, with ageing [16] and due to neurodegenerative disease like Alzheimer's, amyotrophic lateral sclerosis, schizophrenia [114],[115], [116]. Application of rs-fMRI in the identification of neurodegenerative disease is highly characterised by the type of BOLD signal available for analysis which, therefore, indicate the need for obtaining a desired noise-free BOLD signal.

Bibliography

[1] K. Murphy, R. M. Birn, and P. A. Bandettini, "Resting-state fMRI confounds and cleanup," *NeuroImage*, vol. 80, pp. 349–359, 2013.

[2] B. T. Yeo, F. M. Krienen, J. Sepulcre, M. R. Sabuncu, D. Lashkari, M. Hollinshead, J. L. Roffman, J. W. Smoller, L. Zöllei, J. R. Polimeni *et al.*, "The organization of the human cerebral cortex estimated by intrinsic functional connectivity," *Journal of Neurophysiology*, 2011.

[3] T. R. Collins, "Neurologic diseases found to be the largest cause of disability worldwide," *Neurology Today*, vol. 17, no. 22, Nov 2017.

[4] M. Ettcheto, O. Busquets, T. Espinosa-Jiménez, E. Verdaguer, C. Auladell, and A. Camins, "A chronological review of potential disease-modifying therapeutic strategies for Alzheimer's disease," *Current pharmaceutical design*, vol. 26, no. 12, pp. 1286–1299, 2020.

[5] A. Association *et al.*, "2018 Alzheimer's disease facts and figures," *Alzheimer's & Dementia*, vol. 14, no. 3, pp. 367–429, 2018.

[6] A. Halfin, "Depression: the benefits of early and appropriate treatment," *American Journal of Managed Care*, vol. 13, no. 4, p. S92, 2007.

[7] M. Politis and P. Piccini, "Positron emission tomography imaging in neurological disorders," *Journal of Neurology*, vol. 259, no. 9, pp. 1769–1780, 2012.

[8] M. H. Lee, C. D. Smyser, and J. S. Shimony, "Resting-state fMRI: a review of methods and clinical applications," *American Journal of Neuroradiology*, vol. 34, no. 10, pp. 1866–1872, 2013.

[9] F. A. Alturki, K. AlSharabi, A. M. Abdurraqeeb, and M. Aljalal, "EEG signal analysis for diagnosing neurological disorders using discrete wavelet transform and intelligent techniques," *Sensors*, vol. 20, no. 9, p. 2505, 2020.

[10] S. A. Huettel, "Event-related fMRI in cognition," *NeuroImage*, vol. 62, no. 2, pp. 1152–1156, 2012.

[11] B. Biswal, F. Zerrin Yetkin, V. M. Haughton, and J. S. Hyde, "Functional connectivity in the motor cortex of resting human brain using echo-planar MRI," *Magnetic Resonance in Medicine*, vol. 34, no. 4, pp. 537–541, 1995.

[12] D. J. Lurie, D. Kessler, D. S. Bassett, R. F. Betzel, M. Breakspear, S. Kheilholz, A. Kucyi, R. Liégeois, M. A. Lindquist, A. R. McIntosh *et al.*, "Questions and controversies in the study of time-varying functional connectivity in resting fMRI," *Network Neuroscience*, vol. 4, no. 1, pp. 30–69, 2020.

[13] C. S. Monk, S. J. Peltier, J. L. Wiggins, S.-J. Weng, M. Carrasco, S. Risi, and C. Lord, "Abnormalities of intrinsic functional connectivity in autism spectrum disorders," *NeuroImage*, vol. 47, no. 2, pp. 764–772, 2009.

[14] J. Cao, X. Chen, J. Chen, M. Ai, Y. Gan, W. Wang, Z. Lv, S. Zhang, S. Zhang, S. Wang *et al.*, "Resting-state functional MRI of abnormal baseline brain activity in young depressed patients with and without suicidal behavior," *Journal of Affective Disorders*, vol. 205, pp. 252–263, 2016.

[15] N. Khalili-Mahani, R. M. Zoethout, C. F. Beckmann, E. Baerends, M. L. de Kam, R. P. Soeter, A. Dahan, M. A. van Buchem, J. M. van Gerven, and S. A. Rombouts, "Effects of morphine and alcohol on functional brain connectivity during "resting state": A placebo-controlled crossover study in healthy young men," *Human Brain Mapping*, vol. 33, no. 5, pp. 1003–1018, 2012.

[16] F. Barkhof, S. Haller, and S. A. Rombouts, "Resting-state functional MR imaging: a new window to the brain," *Radiology*, vol. 272, no. 1, pp. 29–49, 2014.

[17] T. T. Liu, "Noise contributions to the fMRI signal: An overview," *NeuroImage*, vol. 143, pp. 141–151, 2016.

[18] D. S. Marcus, M. P. Harms, A. Z. Snyder, M. Jenkinson, J. A. Wilson, M. F. Glasser, D. M. Barch, K. A. Archie, G. C. Burgess, M. Ramaratnam *et al.*, "Human Connectome Project informatics: quality control, database services, and data visualization," *NeuroImage*, vol. 80, pp. 202–219, 2013.

[19] L. Griffanti, O. Dipasquale, M. M. Laganà, R. Nemni, M. Clerici, S. M. Smith, G. Baselli, and F. Baglio, "Effective artifact removal in resting state fMRI data improves detection of DMN functional connectivity alteration in Alzheimer's disease," *Frontiers in Human Neuroscience*, vol. 9, p. 449, 2015.

[20] C. M. Bennett, M. B. Miller, and G. L. Wolford, "Neural correlates of interspecies perspective taking in the post-mortem atlantic salmon: An argument for multiple comparisons correction," *NeuroImage*, vol. 47, no. Suppl 1, p. S125, 2009.

[21] M. A. Lindquist, S. Geuter, T. D. Wager, and B. S. Caffo, "Modular preprocessing pipelines can reintroduce artifacts into fMRI data," *Human Brain Mapping*, vol. 40, no. 8, pp. 2358–2376, 2019.

[22] C. W. Granger and R. Joyeux, "An introduction to long-memory time series models and fractional differencing," *Journal of Time Series Analysis*, vol. 1, no. 1, pp. 15–29, 1980.

[23] R. Magin, M. D. Ortigueira, I. Podlubny, and J. Trujillo, "On the fractional signals and systems," *Signal Processing*, vol. 91, no. 3, pp. 350–371, 2011.

[24] A. Eke, P. Herman, J. Bassingthwaighte, G. Raymond, D. Percival, M. Cannon, I. Balla, and C. Ikrényi, "Physiological time series: distinguishing fractal noises from motions," *Pflügers Archiv: European Journal of Physiology*, vol. 439, no. 4, pp. 403–415, 2000.

[25] D. Song, D. Chang, J. Zhang, Q. Ge, Y.-F. Zang, and Z. Wang, "Associations of brain entropy (BEN) to cerebral blood flow and fractional amplitude of low-frequency fluctuations in the resting brain," *Brain Imaging and Behavior*, vol. 13, no. 5, pp. 1486–1495, 2019.

[26] O. Dona, M. D. Noseworthy, C. DeMatteo, and J. F. Connolly, "Fractal analysis of brain blood oxygenation level dependent (BOLD) signals from children with mild traumatic brain injury (mTBI)," *PLoS One*, vol. 12, no. 1, p. e0169647, 2017.

[27] P. Herman, B. G. Sanganahalli, F. Hyder, and A. Eke, "Fractal analysis of spontaneous fluctuations of the BOLD signal in rat brain," *NeuroImage*, vol. 58, no. 4, pp. 1060–1069, 2011.

[28] K. Wang, M. P. van Meer, K. van der Marel, A. van der Toorn, L. Xu, Y. Liu, M. A. Viergever, T. Jiang, and R. M. Dijkhuizen, "Temporal scaling properties and spatial synchronization of spontaneous BOLD signal fluctuations in rat sensorimotor network at different levels of isoflurane anesthesia," *NMR in Biomedicine*, vol. 24, no. 1, p. 29, 2011.

[29] K. Liu, Y. Chen, and X. Zhang, "An evaluation of ARFIMA (autoregressive fractional integral moving average) programs," *Axioms*, vol. 6, no. 2, p. 16, 2017.

[30] P. T. Callaghan, *Principles of Nuclear Magnetic Resonance Microscopy*. Oxford University Press on Demand, 1993.

[31] J. L. Prince and J. M. Links, *Medical Imaging Signals and Systems*. Pearson Prentice Hall Upper Saddle River, 2006.

[32] S. Ogawa, T.-M. Lee, A. S. Nayak, and P. Glynn, "Oxygenation-sensitive contrast in magnetic resonance image of rodent brain at high magnetic fields," *Magnetic Resonance in Medicine*, vol. 14, no. 1, pp. 68–78, 1990.

[33] S. Ogawa, T.-M. Lee, A. R. Kay, and D. W. Tank, "Brain magnetic resonance imaging with contrast dependent on blood oxygenation," *Proceedings of the National Academy of Sciences*, vol. 87, no. 24, pp. 9868–9872, 1990.

[34] D. Attwell and S. B. Laughlin, "An energy budget for signaling in the grey matter of the brain," *Journal of Cerebral Blood Flow & Metabolism*, vol. 21, no. 10, pp. 1133–1145, 2001.

[35] P. A. Bandettini, E. C. Wong, R. S. Hinks, R. S. Tikofsky, and J. S. Hyde, "Time course EPI of human brain function during task activation," *Magnetic Resonance in Medicine*, vol. 25, no. 2, pp. 390–397, 1992.

[36] R. D. Hoge, J. Atkinson, B. Gill, G. R. Crelier, S. Marrett, and G. B. Pike, "Linear coupling between cerebral blood flow and oxygen consumption in activated human cortex," *Proceedings of the National Academy of Sciences*, vol. 96, no. 16, pp. 9403–9408, 1999.

[37] N. K. Logothetis, J. Pauls, M. Augath, T. Trinath, and A. Oeltermann, "Neurophysiological investigation of the basis of the fMRI signal," *Nature*, vol. 412, no. 6843, pp. 150–157, 2001.

[38] R. A. Poldrack, J. A. Mumford, and T. E. Nichols, *Handbook of functional MRI data analysis*. Cambridge University Press, 2011.

[39] R. M. Birn, J. B. Diamond, M. A. Smith, and P. A. Bandettini, "Separating respiratory-variation-related fluctuations from neuronal-activity-related fluctuations in fMRI," *NeuroImage*, vol. 31, no. 4, pp. 1536–1548, 2006.

[40] C. Caballero-Gaudes and R. C. Reynolds, "Methods for cleaning the BOLD fMRI signal," *NeuroImage*, vol. 154, pp. 128–149, 2017.

[41] J. D. Power, M. Plitt, S. J. Gotts, P. Kundu, V. Voon, P. A. Bandettini, and A. Martin, "Ridding fMRI data of motion-related influences: Removal of signals with distinct spatial and physical bases in multiecho data," *Proceedings of the National Academy of Sciences*, vol. 115, no. 9, pp. E2105–E2114, 2018.

[42] K. R. Van Dijk, M. R. Sabuncu, and R. L. Buckner, "The influence of head motion on intrinsic functional connectivity MRI," *NeuroImage*, vol. 59, no. 1, pp. 431–438, 2012.

[43] C. Chang, J. P. Cunningham, and G. H. Glover, "Influence of heart rate on the BOLD signal: the cardiac response function," *NeuroImage*, vol. 44, no. 3, pp. 857–869, 2009.

[44] K. J. Friston, S. Williams, R. Howard, R. S. Frackowiak, and R. Turner, "Movement-related effects in fMRI time-series," *Magnetic Resonance in Medicine*, vol. 35, no. 3, pp. 346–355, 1996.

[45] T. D. Satterthwaite, M. A. Elliott, R. T. Gerraty, K. Ruparel, J. Loughead, M. E. Calkins, S. B. Eickhoff, H. Hakonarson, R. C. Gur, R. E. Gur *et al.*, "An improved framework for confound regression and filtering for control of motion artifact in the preprocessing of resting-state functional connectivity data," *NeuroImage*, vol. 64, pp. 240–256, 2013.

[46] P. Kundu, S. J. Inati, J. W. Evans, W.-M. Luh, and P. A. Bandettini, "Differentiating BOLD and non-BOLD signals in fMRI time series using multi-echo EPI," *NeuroImage*, vol. 60, no. 3, pp. 1759–1770, 2012.

[47] G. E. Box, G. M. Jenkins, G. C. Reinsel, and G. M. Ljung, *Time Series Analysis: Forecasting and Control*. John Wiley & Sons, 2015.

[48] R. H. Shumway, D. S. Stoffer, and D. S. Stoffer, *Time Series Analysis and Its Applications*. Springer, 2000, vol. 3.

[49] C. S. Smith and M. Verhaegen, *Lecture Notes SC42150: Statistical Signal Processing*. Delft University of Technology, 2020.

[50] J. Xiu and Y. Jin, "Empirical study of ARFIMA model based on fractional differencing," *Physica A: Statistical Mechanics and its Applications*, vol. 377, no. 1, pp. 138–154, 2007.

[51] A. A. Kilbas, H. M. Srivastava, and J. J. Trujillo, *Theory and Applications of Fractional Differential Equations*. Elsevier, 2006, vol. 204.

[52] R. L. Magin, "Fractional calculus in bioengineering, part 1," *Critical Reviews™ in Biomedical Engineering*, vol. 32, no. 1, 2004.

[53] K. Torre, D. Delignières, and L. Lemoine, "Detection of long-range dependence and estimation of fractal exponents through ARFIMA modelling," *British Journal of Mathematical and Statistical Psychology*, vol. 60, no. 1, pp. 85–106, 2007.

[54] G. B. Arfken, H. J. Weber, and F. E. Harris, "Chapter 13 - gamma function," in *Mathematical Methods for Physicists*, seventh edition ed. Academic Press, 2013, pp. 599–641.

[55] S. Lopes, B. Olbermann, and V. Reisen, "A comparison of estimation methods in non-stationary ARFIMA processes," *Journal of Statistical Computation and Simulation*, vol. 74, no. 5, pp. 339–347, 2004.

[56] V. Reisen, B. Abraham, and S. Lopes, "Estimation of parameters in ARFIMA processes: A simulation study," *Communications in Statistics-Simulation and Computation*, vol. 30, no. 4, pp. 787–803, 2001.

[57] S. M. Smith, C. F. Beckmann, J. Andersson, E. J. Auerbach, J. Bijsterbosch, G. Douaud, E. Duff, D. A. Feinberg, L. Griffanti, M. P. Harms *et al.*, "Resting-state fMRI in the human connectome project," *NeuroImage*, vol. 80, pp. 144–168, 2013.

[58] D. C. Van Essen, S. M. Smith, D. M. Barch, T. E. Behrens, E. Yacoub, K. Ugurbil, W.-M. H. Consortium *et al.*, "The WU-Minn Human Connectome Project: an overview," *NeuroImage*, vol. 80, pp. 62–79, 2013.

[59] N. Tzourio-Mazoyer, B. Landeau, D. Papathanassiou, F. Crivello, O. Etard, N. Delcroix, B. Mazoyer, and M. Joliot, "Automated anatomical labeling of activations in SPM using a macroscopic anatomical parcellation of the MNI MRI single-subject brain," *NeuroImage*, vol. 15, no. 1, pp. 273–289, 2002.

[60] J. Talairach, "Co-planar stereotaxic atlas of the human brain-3-dimensional proportional system," *An Approach to Cerebral Imaging*, 1988.

[61] R. A. Poldrack, "Region of interest analysis for fMRI," *Social Cognitive and Affective Neuroscience*, vol. 2, no. 1, pp. 67–70, 2007.

[62] A. Schaefer, R. Kong, E. M. Gordon, T. O. Laumann, X.-N. Zuo, A. J. Holmes, S. B. Eickhoff, and B. T. Yeo, "Local-global parcellation of the human cerebral cortex from intrinsic functional connectivity MRI," *Cerebral Cortex*, vol. 28, no. 9, pp. 3095–3114, 2018.

[63] G. Salimi-Khorshidi, G. Douaud, C. F. Beckmann, M. F. Glasser, L. Griffanti, and S. M. Smith, "Automatic denoising of functional MRI data: combining independent component analysis and hierarchical fusion of classifiers," *NeuroImage*, vol. 90, pp. 449–468, 2014.

[64] L. Griffanti, G. Salimi-Khorshidi, C. F. Beckmann, E. J. Auerbach, G. Douaud, C. E. Sexton, E. Zsoldos, K. P. Ebmeier, N. Filippini, C. E. Mackay *et al.*, "ICA-based artefact removal and accelerated fMRI acquisition for improved resting state network imaging," *NeuroImage*, vol. 95, pp. 232–247, 2014.

[65] C. F. Beckmann and S. M. Smith, "Probabilistic independent component analysis for functional magnetic resonance imaging," *IEEE Transactions on Medical Imaging*, vol. 23, no. 2, pp. 137–152, 2004.

[66] A. E. Desjardins, K. A. Kiehl, and P. F. Liddle, "Removal of confounding effects of global signal in functional MRI analyses," *NeuroImage*, vol. 13, no. 4, pp. 751–758, 2001.

[67] D. Kwiatkowski, P. C. Phillips, P. Schmidt, and Y. Shin, "Testing the null hypothesis of stationarity against the alternative of a unit root: How sure are we that economic time series have a unit root?" *Journal of Econometrics*, vol. 54, no. 1-3, pp. 159–178, 1992.

[68] C. Gorrostieta, M. Fiecas, H. Ombao, E. Burke, and S. Cramer, "Hierarchical vector auto-regressive models and their applications to multi-subject effective connectivity," *Frontiers in Computational Neuroscience*, vol. 7, p. 159, 2013.

[69] Student, "The probable error of a mean," *Biometrika*, pp. 1–25, 1908.

[70] R. K. Niazy, J. Xie, K. Miller, C. F. Beckmann, and S. M. Smith, "Spectral characteristics of resting state networks," *Progress in Brain Research*, vol. 193, pp. 259–276, 2011.

[71] K. Kalcher, R. N. Boubela, W. Huf, L. Bartova, C. Kronnerwetter, B. Derntl, L. Pezawas, P. Filzmoser, C. Nasel, and E. Moser, "The spectral diversity of resting-state fluctuations in the human brain," *PLoS One*, vol. 9, no. 4, p. e93375, 2014.

[72] R. M. Birn, M. A. Smith, T. B. Jones, and P. A. Bandettini, "The respiration response function: the temporal dynamics of fMRI signal fluctuations related to changes in respiration," *NeuroImage*, vol. 40, no. 2, pp. 644–654, 2008.

[73] F. Nikolaou, C. Orphanidou, P. Papakyriakou, K. Murphy, R. G. Wise, and G. D. Mitsis, "Spontaneous physiological variability modulates dynamic functional connectivity in resting-state functional magnetic resonance imaging," *Philosophical Transactions of the Royal Society A: Mathematical, Physical and Engineering Sciences*, vol. 374, no. 2067, p. 20150183, 2016.

[74] N. H. Yuen, N. Osachoff, and J. J. Chen, "Intrinsic frequencies of the resting-state fMRI signal: the frequency dependence of functional connectivity and the effect of mode mixing," *Frontiers in Neuroscience*, vol. 13, p. 900, 2019.

[75] F. J. Massey Jr, "The Kolmogorov-Smirnov test for goodness of fit," *Journal of the American statistical Association*, vol. 46, no. 253, pp. 68–78, 1951.

[76] M. D. Greicius, G. Srivastava, A. L. Reiss, and V. Menon, "Default-mode network activity distinguishes Alzheimer's disease from healthy aging: evidence from functional MRI," *Proceedings of the National Academy of Sciences*, vol. 101, no. 13, pp. 4637–4642, 2004.

[77] S. A. Rombouts, J. S. Damoiseaux, R. Goekoop, F. Barkhof, P. Scheltens, S. M. Smith, and C. F. Beckmann, "Model-free group analysis shows altered BOLD fMRI networks in dementia," *Human Brain Mapping*, vol. 30, no. 1, pp. 256–266, 2009.

[78] A. Anand, Y. Li, Y. Wang, J. Wu, S. Gao, L. Bukhari, V. P. Mathews, A. Kalnin, and M. J. Lowe, "Activity and connectivity of brain mood regulating circuit in depression: a functional magnetic resonance study," *Biological Psychiatry*, vol. 57, no. 10, pp. 1079–1088, 2005.

[79] Y. Liu, M. Liang, Y. Zhou, Y. He, Y. Hao, M. Song, C. Yu, H. Liu, Z. Liu, and T. Jiang, "Disrupted small-world networks in schizophrenia," *Brain*, vol. 131, no. 4, pp. 945–961, 2008.

[80] C. Grefkes, D. A. Nowak, S. B. Eickhoff, M. Dafotakis, J. Küst, H. Karbe, and G. R. Fink, "Cortical connectivity after subcortical stroke assessed with functional magnetic resonance imaging," *Annals of Neurology*, vol. 63, no. 2, pp. 236–246, 2008.

[81] W. Liao, Z. Zhang, Z. Pan, D. Mantini, J. Ding, X. Duan, C. Luo, G. Lu, and H. Chen, "Altered functional connectivity and small-world in mesial temporal lobe epilepsy," *PLoS One*, vol. 5, no. 1, p. e8525, 2010.

[82] M. B. Wang, J. P. Owen, P. Mukherjee, and A. Raj, "Brain network eigenmodes provide a robust and compact representation of the structural connectome in health and disease," *PLoS Computational Biology*, vol. 13, no. 6, p. e1005550, 2017.

[83] A. Neumaier and T. Schneider, "Estimation of parameters and eigenmodes of multivariate autoregressive models," *ACM Transactions on Mathematical Software (TOMS)*, vol. 27, no. 1, pp. 27–57, 2001.

[84] M. Parsian, *Data Algorithms: Recipes for Scaling Up with Hadoop and Spark.* " O'Reilly Media, Inc.", 2015.

[85] M. Hollander, D. A. Wolfe, and E. Chicken, *Nonparametric Statistical Methods.* John Wiley & Sons, 2013, vol. 751.

[86] M. D. Fox and M. E. Raichle, "Spontaneous fluctuations in brain activity observed with functional magnetic resonance imaging," *Nature Reviews Neuroscience*, vol. 8, no. 9, pp. 700–711, 2007.

[87] Y. Tong, L. M. Hocke, and B. B. Frederick, "Low frequency systemic hemodynamic "noise" in resting state BOLD fMRI: characteristics, causes, implications, mitigation strategies, and applications," *Frontiers in Neuroscience*, vol. 13, p. 787, 2019.

[88] G. W. Corder and D. I. Foreman, "Nonparametric statistics for Non-Statisticians," 2011.

[89] M. D. Fox, A. Z. Snyder, J. L. Vincent, M. Corbetta, D. C. Van Essen, and M. E. Raichle, "The human brain is intrinsically organized into dynamic, anticorrelated functional networks," *Proceedings of the National Academy of Sciences*, vol. 102, no. 27, pp. 9673–9678, 2005.

[90] P. Fransson, "Spontaneous low-frequency BOLD signal fluctuations: An fMRI investigation of the resting-state default mode of brain function hypothesis," *Human Brain Mapping*, vol. 26, no. 1, pp. 15–29, 2005.

[91] R. Boyacioglu, C. F. Beckmann, and M. Barth, "An investigation of RSN frequency spectra using ultra-fast generalized inverse imaging," *Frontiers in Human Neuroscience*, vol. 7, p. 156, 2013.

[92] R. N. Boubela, K. Kalcher, W. Huf, C. Kronnerwetter, P. Filzmoser, and E. Moser, "Beyond noise: using temporal ICA to extract meaningful information from high-frequency fMRI signal fluctuations during rest," *Frontiers in Human Neuroscience*, vol. 7, p. 168, 2013.

[93] A. Ashourvan, S. Pequito, M. Bertolero, J. Z. Kim, D. S. Bassett, and B. Litt, "A dynamical systems framework to uncover the drivers of large-scale cortical activity," *bioRxiv*, p. 638718, 2019.

[94] G. Deshpande, S. LaConte, G. A. James, S. Peltier, and X. Hu, "Multivariate granger causality analysis of fMRI data," *Human Brain Mapping*, vol. 30, no. 4, pp. 1361–1373, 2009.

[95] C. Büchel and K. J. Friston, "Modulation of connectivity in visual pathways by attention: cortical interactions evaluated with structural equation modelling and fMRI." *Cerebral Cortex (New York, NY: 1991)*, vol. 7, no. 8, pp. 768–778, 1997.

[96] J. Yan, Y. Wang, G. Ouyang, T. Yu, Y. Li, A. Sik, and X. Li, "Analysis of electrocorticogram in epilepsy patients in terms of criticality," *Nonlinear Dynamics*, vol. 83, no. 4, pp. 1909–1917, 2016.

[97] M. Scheffer, J. Bascompte, W. A. Brock, V. Brovkin, S. R. Carpenter, V. Dakos, H. Held, E. H. Van Nes, M. Rietkerk, and G. Sugihara, "Early-warning signals for critical transitions," *Nature*, vol. 461, no. 7260, pp. 53–59, 2009.

[98] K. J. Friston, "Functional and Effective Connectivity: A Review," *Brain Connectivity*, vol. 1, no. 1, pp. 13–36, 2011.

[99] W. D. Penny, K. J. Friston, J. T. Ashburner, S. J. Kiebel, and T. E. Nichols, *Statistical Parametric Mapping: The Analysis of Functional Brain Images*. Elsevier, 2011.

[100] C. Chang and G. H. Glover, "Time-frequency dynamics of resting-state brain connectivity measured with fMRI," *NeuroImage*, vol. 50, no. 1, pp. 81–98, 2010.

[101] R. M. Hutchison, T. Womelsdorf, E. A. Allen, P. A. Bandettini, V. D. Calhoun, M. Corbetta, S. Della Penna, J. H. Duyn, G. H. Glover, J. Gonzalez-Castillo *et al.*, "Dynamic functional connectivity: Promise, issues, and interpretations," *NeuroImage*, vol. 80, pp. 360–378, 2013.

[102] M. G. Preti, T. A. Bolton, and D. Van De Ville, "The dynamic functional connectome: State-of-the-art and perspectives," *NeuroImage*, vol. 160, pp. 41–54, 2017.

[103] G. S. Wig, B. L. Schlaggar, and S. E. Petersen, "Concepts and principles in the analysis of brain networks," *Annals of the New York Academy of Sciences*, vol. 1224, no. 1, pp. 126–146, 2011.

[104] B. Colombo, M. A. Rocca, R. Messina, S. Guerrieri, and M. Filippi, "Resting-state fMRI functional connectivity: a new perspective to evaluate pain modulation in migraine?" *Neurological Sciences*, vol. 36, no. 1, pp. 41–45, 2015.

[105] C. F. Beckmann, M. DeLuca, J. T. Devlin, and S. M. Smith, "Investigations into resting-state connectivity using independent component analysis," *Philosophical Transactions of the Royal Society B: Biological Sciences*, vol. 360, no. 1457, pp. 1001–1013, 2005.

[106] J. S. Damoiseaux and M. D. Greicius, "Greater than the sum of its parts: a review of studies combining structural connectivity and resting-state functional connectivity," *Brain Structure and Function*, vol. 213, no. 6, pp. 525–533, 2009.

[107] M. De Luca, C. F. Beckmann, N. De Stefano, P. M. Matthews, and S. M. Smith, "fMRI resting state networks define distinct modes of long-distance interactions in the human brain," *NeuroImage*, vol. 29, no. 4, pp. 1359–1367, 2006.

[108] M. P. Van Den Heuvel and H. E. H. Pol, "Exploring the brain network: a review on resting-state fMRI functional connectivity," *European Neuropsychopharmacology*, vol. 20, no. 8, pp. 519–534, 2010.

[109] M. E. Raichle, "The restless brain," *Brain Connectivity*, vol. 1, no. 1, pp. 3–12, 2011.

[110] M. E. Raichle and A. Z. Snyder, "A default mode of brain function: a brief history of an evolving idea," *NeuroImage*, vol. 37, no. 4, pp. 1083–1090, 2007.

[111] K. R. Van Dijk, T. Hedden, A. Venkataraman, K. C. Evans, S. W. Lazar, and R. L. Buckner, "Intrinsic functional connectivity as a tool for human connectomics: theory, properties, and optimization," *Journal of Neurophysiology*, vol. 103, no. 1, pp. 297–321, 2010.

[112] R. L. Buckner, J. R. Andrews-Hanna, and D. L. Schacter, "The brain's default network: anatomy, function, and relevance to disease." *Annals of the New York Academy of Sciences*, 2008.

[113] M. D. Greicius, B. Krasnow, A. L. Reiss, and V. Menon, "Functional connectivity in the resting brain: a network analysis of the default mode hypothesis," *Proceedings of the National Academy of Sciences*, vol. 100, no. 1, pp. 253–258, 2003.

[114] S. A. Rombouts, F. Barkhof, R. Goekoop, C. J. Stam, and P. Scheltens, "Altered resting state networks in mild cognitive impairment and mild Alzheimer's disease: an fMRI study," *Human Brain Mapping*, vol. 26, no. 4, pp. 231–239, 2005.

[115] B. Mohammadi, K. Kollewe, A. Samii, K. Krampfl, R. Dengler, and T. F. Münte, "Changes of resting state brain networks in amyotrophic lateral sclerosis," *Experimental Neurology*, vol. 217, no. 1, pp. 147–153, 2009.

[116] W. Guo, D. Yao, J. Jiang, Q. Su, Z. Zhang, J. Zhang, L. Yu, and C. Xiao, "Abnormal default-mode network homogeneity in first-episode, drug-naive schizophrenia at rest," *Progress in Neuro-Psychopharmacology and Biological Psychiatry*, vol. 49, pp. 16–20, 2014.

Glossary

List of Acronyms

BOLD	blood-oxygen-level-dependent
fMRI	functional magnetic resonance imaging
rs-fMRI	resting-state fMRI
rs-BOLD	resting-state BOLD
FC	functional connectivity
WSS	Wide Sense Stationary
LRD	long-range dependence
ARFIMA	Autoregressive Fractional Integral Moving Average
ARMA	Autoregressive Moving Average
ROI	region of interest
ROIs	Regions of Interest
ACF	Autocorrelation Function